Title	Formation of an ultracarbonaceous Antarctic micrometeorite through minimal aqueous alteration in a small porous icy body
Auther(s)	Yabuta, Hikaru; Noguchi, Takaaki; Itoh, Shoichi; Nakamura, Tomoki; Miyake, Akira; Shinichi, Tsujimoto; Ohashi, Noriaki; Sakamoto, Naoya; Hashiguchi, Minako; Abe, Ken-ichi; Okubo, Aya; Kilcoyne, A. L. David; Tachibana, Shogo; Okazaki, Ryuji; Terada, Kentaro; Ebihara, Mitsuru; Nagahara, Hiroko
Citation	Geochimica et Cosmochimica Acta , 214 : 172 - 190
Issue Date	2017-10-01
DOI	10.1016/j.gca.2017.06.047
Self DOI	
URL	http://ir.lib.hiroshima-u.ac.jp/00048703
Right	© 2017. This manuscript version is made available under the CC-BY-NC-ND 4.0 license http://creativecommons.org/licenses/by-nc-nd/4.0/ This is not the published version. Please cite only the published version. この論文は出版社版でありません。引用の際には出版社版をご確認、ご利用ください。
Relation	


HiR
Hiroshima University Institutional Repository

Formation of an Ultracarbonaceous Antarctic Micrometeorite through Minimum Aqueous Alteration in a Small Porous Icy Body

Hikaru Yabuta[1 †], Takaaki Noguchi[2], Shoichi Itoh[3], Tomoki Nakamura[4], Akira Miyake[3], Shinichi Tsujimoto[5], Noriaki Ohashi[5], Naoya Sakamoto[6], Minako Hashiguchi[7], Ken-ichi Abe[6], Aya Okubo[8], A. L. David Kilcoyne[9], Shogo Tachibana[6], Ryuji Okazaki[7], Kentaro Terada[10], Mitsuru Ebihara[11] and Hiroko Nagahara[8]

[1] Department of Earth and Planetary Systems Science, Hiroshima University, 1-3-1 Kagamiyama, Hiroshima 739-8526, Japan

[2] Faculty of Arts and Science, Kyushu University, 744 Motooka, Nishi-ku, Fukuoka 819-0395, Japan

[3] Faculty of Science, Kyoto University, Kitashirakawa Oiwake-cho, Sakyo-ku, Kyoto 606-8502, Japan

[4] Department of Earth Science, Tohoku University, 6-3 Aramaki Aza Aoba, Aoba, Sendai,

Miyagi 980-8578, Japan

[5] College of Science, Ibaraki University, 2-1-1, Bunkyo, Mito, 310-8512, Japan

[6] Department of Natural History Sciences, Hokkaido University, N10W8, Kita-ku, Sapporo 060-0810, Japan

[7] Faculty of Science, Kyushu University, 744 Motooka, Nishi-ku, Fukuoka 819-0395, Japan

[8] Department of Earth and Planetary Science, The University of Tokyo, 7-3-1 Hongo, Bunkyo-ku, Tokyo 113-0033 Japan

[9] Advanced Light Source, Lawrence Berkeley National Laboratory, 6 Cyclotron Rd., Berkeley, CA 94720, USA

[10] Department of Earth and Space Science, Osaka University, 1-1 Machikaneyama, Toyonaka, Osaka 560-0043, Japan

[11] Department of Chemistry, Tokyo Metropolitan University, 1-1 Minami-Osawa, Hachioji, Tokyo 192-0397, Japan

[†]Corresponding author: Tel: +81-82-424-7474; Fax: +81-82-424-0735

E-mail address: hyabuta@hiroshima-u.ac.jp

35 *Keywords: Ultracarbonaceous Antarctic micrometeorites, organic matter, GEMS, aqueous*
36 *alteration, comet, shock, SIMS, XANES, TEM*

37

38

39 **Abstract**

40 A comprehensive study of organic chemistry and mineralogy of an ultracarbonaceous
41 micrometeorite (UCAMM D05IB80), collected from near the Dome Fuji Station, Antarctica,
42 has been carried out in order to understand the genetic relationship among organic materials,
43 silicates, and water. The micrometeorite is composed of a dense aggregate of ~5-μm-sized
44 hollow ellipsoidal organic material containing submicrometer-sized phases such as GEMS
45 and mineral grains. There is a wide area of organic material (~15 x 15 μm) in its interior.
46 Low-Ca pyroxene is much more abundant than olivine and shows various Mg/(Mg+Fe) ratios
47 from ~1.0 to 0.78, which is common to previous works of UCAMM. By contrast, GEMS
48 grains in this UCAMM have unusual chemical compositions. They are depleted in both Mg
49 and S, which suggests that these elements were leached out from the GEMS grains during
50 very weak aqueous alteration without forming phyllosilicates.

51 The organics show two types of texture, smooth and globular with an irregular outline,
52 and both of them are composed of imine, nitrile and/or aromatic nitrogen heterocycles, and

53 amide. The ratio of nitrogen to carbon (N/C) in the smooth region of the organics is ~0.15,
54 which is five times higher than insoluble organic macromolecules in types 1 and 2 chondritic
55 meteorites. In addition, the UCAMM organics is soluble in epoxy, and thus it has
56 hydrophilicity. These polar natures indicate that the organic material in the UCAMM is very
57 primitive. The surface of the organics is coated with an inorganic layer with a few nanometers
58 thickness, which consists of C, O, Si, S, and Fe. Sulfur is also contained in the interior,
59 implying the presence of organosulfur moieties. There is no isotopic anomaly of D, ^{13}C and
60 ^{15}N in the organic material.

61 Since interstellar photochemistry alone would not be able to explain the N/C ratio of the
62 UCAMM organics, we suggest that very small amount of fluid on a comet must have been
63 necessary for the formation of UCAMM. The GEMS grains depleted in Mg and S in the
64 UCAMM prove a very weak degree of aqueous alteration, which is weaker than that of
65 carbonaceous chondrites. Short-duration weak alteration probably caused by planetesimal
66 shock locally melts cometary ice grains and releases water that dissolves organics, while the
67 fluid unlikely mobilizes because of very low thermal conductivity of the porous icy body.
68 This event allows formation of a large organic puddle of the UCAMM, as well as organic
69 matter sulfurization, formation of mineral membrane-like thin layers, and deformation of

70 organic nanoglobules.

71 **(408 words (max. 500 words))**

72

73 **1. Introduction**

74 Interstellar dusts that accreted to form a protoplanetary disk are thought to be
75 micron-sized particles consisting of an amorphous silicate core, a refractory organic mantle,
76 and an outer mantle of ice (Greenberg and Li, 1997). Because of the large difference in the
77 thermal stability of these three components, the grains are expected to change their
78 composition according to thermal processing in a protoplanetary disk. The association of
79 reactive components, amorphous silicates, organic materials, and water, in a single grain
80 suggests possible interactions among the three components. It has been recently well
81 recognized that organic materials in chondrites were the aqueously and/or thermally
82 processed products in parent bodies and that their chemical and isotopic signatures were
83 modified (e.g., Alexander et al., 2007). It is, however, not known what the precursor materials
84 were and under what the conditions organics were processed in chondrite parent bodies.
85 Therefore, it is important to trace back to the evolution and interactions among silicates and
86 organic materials, and ice in the proto-solar disk and their consequence in parent bodies. It
87 requires us to study organics as primitive as possible, which might correspond to the materials
88 other than those found in chondrites.

89 Interplanetary dust particles (IDPs) and Antarctic micrometeorites (AMMs) are one of the

most primitive Solar System materials available to us and one of the most suitable objects for an *in-situ* study on the origin of and spatial relationship between organic and inorganic materials formed in the early Solar System. Chondritic porous (CP)-IDPs are thought to have a link with short period comets (Messenger et al. 2006), based on their fine-grained, porous, and fragile structure (Bradley and Brownlee, 1986), high abundance of carbon (~12%, Thomas et al. 1994), and the presence of sub-micron silicate glass with embedded metal and sulfides (GEMS) (Bradley et al. 1999). It has been also known that D- and ^{15}N- enrichments of the organics in CP-IDPs (e.g., Messenger, 2000; Floss et al. 2004) and IDPs from the comet 26P/Grigg–Skjellerup dust stream (Busemann et al. 2009) resemble those found in the primitive types 1 and 2 carbonaceous chondrites (Busemann et al., 2006; Nakamura-Messenger et al. 2006). Recently, AMMs containing porous aggregates of GEMS and enstatite whisker/platelets, which are similar morphology and mineralogy to CP-IDPs, have been identified (Noguchi et al. 2015). Both IDPs and AMMs are thus the key extraterrestrial materials to enhance our understanding of the relationship between comets and meteorites.

Of the AMMs, ultracarbonaceous micrometeorites (UCAMMs) are unique extraterrestrial materials that contain a large amount of carbonaceous materials. They were collected for the

first time by the 46th and 47th Japan Antarctic Research Expedition (JARE) teams from the virgin surface snow near the Dome Fuji Station, Antarctica, and reported to have pristine nature in terms of mineralogy and chemistry (Nakamura et al. 2005). One of the UCAMMs contains light noble gases with solar wind origin, and two contain high abundance of presolar grains (Yada et al. 2008; Floss et al. 2012). UCAMMs have been independently found in Antarctica by the French-Italian team, which are characterized by D-enrichment in organic matter (Duprat et al. 2010). The degree of D-enrichment is by factors to an order of magnitude larger than the terrestrial value. Duprat et al. (2010) has discussed that organic materials in UCAMMs could be produced in the outer protoplanetary disk, based on the identification of crystalline minerals that are thought to be solar origin and are embedded in the organic material. Dartois et al. (2013) have further reported ^{15}N- and D-rich micrometeorites and have proposed that the nitrogen-rich organic material in UCAMM was formed by irradiation of CH_4 - and N_2 -rich ice in the Oort cloud.

In the present study, we have made a comprehensive mineralogical and organic chemical study of a UCAMM and suggest a new pathway for the formation of UCAMMs through the interaction of organics, silicates, and water in the very early stage of alteration in a parent body.

2. Experimental

The Antarctic snow, collected by the 51st JARE team of the National Institute of Polar Research (NIPR), was melted and filtered in a class 1000 clean room at Ibaraki University, and the residual particles were manually picked up under a binocular microscope. Details of the micrometeorite collecting method are described by Sakamoto et al. (2010). They were observed with JEOL JSM-5600LV scanning electron microscope (SEM) equipped with energy dispersive spectrometer (EDS) at Ibaraki University and micrometeorites were selected from terrestrial materials based on the morphology and EDS spectra with chondritic composition rich in Si, Mg, Fe, and O (see electronic supplementary data, S1). About 90 micrometeorites were identified from fine-grained particles collected from ~100 kg of the snow. When the intensity of C kα peak exceeds twice that of O kα, it was classified as an UCAMM in this study, and only one, D05IB80, was identified as an UCAMM. Bulk mineralogy of D05IB80 was investigated by using synchrotron radiation X-ray diffraction (SR-XRD) at the Photon Factory Institute of Materials Structure Science, High Energy Accelerator Research Organization, Tsukuba, Japan.

Raman spectroscopy of the UCAMM D05IB80 was performed by JASCO NRS-3100

141 Raman spectrometer equipped with the 785-nm excitation laser at Ibaraki University. The
142 beam diameter of the laser was ~ 2 μm, and the laser power was suppressed below 1 mW to
143 avoid decomposition of carbonaceous material.

144 Next, UCAMM D05IB80 was embedded in epoxy resin and ultramicrotomed into
145 70-nm-thick sections. After ultramicrotomy, the potted butt of the micrometeorite was
146 embedded again in epoxy resin and the surface was polished to make a flat epoxy disk (6 mm
147 in diameter) for the isotopic mapping analysis with a SIMS at the Hokkaido University
148 (Cameca ims-1270 SIMS equipped with SCAPS) (Yurimoto et al. 2003). Schematic diagrams
149 to show the 3D relationships among the ultrathin samples (ultramicrotomed sections and a
150 FIB section) and the flat sample of this UCAMM is presented in Fig. A1.

151 A ~100 - ~200 pA Cs^+ primary beam in the aperture illumination mode of SIMS was used
152 to achieve uniform secondary ion emission from a sample area of ~ 30 × 40 μm^2. A normal
153 incident electron gun was used to compensate for sample charging and the exit slit was
154 narrow enough to eliminate the contribution of interference ions to the isotope images.
155 Isotopographs of $^{16}O^-$, $^{12}C^{14}N^-$, $^{32}S^-$, $^{1}H^-$, $^{2}D^-$, $^{1}H^-$, $^{16}O^-$, $^{12}C^{14}N^-$ and $^{32}S^-$ were acquired in this
156 order, where a 150-μm contrast aperture (CA) was applied for H and D isotopographs and a
157 50-μm CA for $^{16}O^-$, $^{12}C^{14}N^-$ and $^{32}S^-$ isotopographs in order to obtain high lateral spatial

158 resolution. The exposure time was 20 s for H^-, 1,000 s for D^-, 20 s for $^{16}O^-$, 20 s for $^{12}C^{14}N^-$

159 and 40 s for $^{32}S^-$, respectively. We obtained secondary ion images of $^{12}C^{14}N^-$, $^{12}C^{15}N^-$, $^{12}C^{14}N^-$,

160 $^{12}C^-$, $^{13}C^-$ and $^{12}C^-$ sequentially for the second session after FIB. A 50 μm CA was used for

161 $^{12}C^{14}N^-$, $^{12}C^{15}N^-$, $^{12}C^-$ and $^{13}C^-$ isotopograph. The exposure time was 50 s for $^{12}C^{14}N^-$, 400 s for

162 $^{12}C^{15}N^-$, 50 s for $^{12}C^-$ and 500 s for $^{13}C^-$.

163 Hydrogen, nitrogen and carbon isotopic composition are represented by δ-value notation;

164 $$\delta D_{SMOW} = \left\{ \frac{(D/H)_{sample}}{(D/H)_{SMOW}} - 1 \right\} \times 1000$$

165 $$\delta^{15}N_{AIR} = \left\{ \frac{(^{15}N/^{14}N)_{sample}}{(^{15}N/^{14}N)_{AIR}} - 1 \right\} \times 1000$$

166 $$\delta^{13}C_{PDB} = \left\{ \frac{(^{13}C/^{12}C)_{sample}}{(^{13}C/^{12}C)_{PDB}} - 1 \right\} \times 1000$$

167 where SMOW denotes the standard mean ocean water, and AIR denotes the Earth's

168 atmosphere and PDB denotes Pee Dee Belemnite. The instrumental mass fractionations for

169 the D/H, $^{15}N/^{14}N$ and $^{13}C/^{12}C$ ratios of epoxy were corrected by assuming that the δD, $\delta^{15}N$

170 and $\delta^{13}C$ values are 0‰, respectively, and that the matrix effects are the same for epoxy and

171 organic matters in the UCAMM. Therefore, the δ-values of the organic matters shown here

172 are the relative values to the epoxy. The isotope ratio image was obtained by averaging 5 x 5

173 pixels (corresponding to 1.0 x 1.0 μm^2) for δD and 3 x 3 pixels (corresponding to 0.6 x 0.6

174 μm^2) for $\delta^{15}N$ and $\delta^{13}C$ in order to reduce the statistical error. Lateral resolutions of the

175 isotopographs are ~1 μm for $^{1}H^{-}$, and $^{2}D^{-}$ and ~0.6 μm for $^{12}C^{-}$, $^{13}C^{-}$, $^{12}C^{14}N^{-}$, $^{12}C^{15}N^{-}$, $^{32}S^{-}$, and

176 $^{16}O^{-}$.

177 The morphology of the UCAMM was observed by FE-SEM-EDS (JSM-7000F, Oxford

178 INCA Energy) system at Hokkaido University after the isotope microscope analyses, and a

179 thin section with 200-nm of thickness was prepared by the dual beam focused ion beam and

180 scanning electron microscope (FIB-SEM) JEOL JIB-4501 at Ibaraki University for further

181 analyses.

182 Carbon (C)-, nitrogen (N)-, and oxygen (O)- X-ray absorption near edge structure

183 (XANES) spectra of the FIB section were acquired by using STXM at the beamline (BL)

184 5.3.2.2. of Advanced Light Source (ALS) at the Lawrence Berkeley National Laboratory

185 (Kilcoyne et al. 2003). The beamline employs a bending magnet providing a useful photon

186 range spanning approximately from 250 to 800 eV with a flux of 10^{7} photons per second.

187 Energy selection on BL5.3.2 is performed with a low dispersion spherical grating

188 monochromator and affording an energy resolution ($E/\Delta E$) of 5000. Carbon-XANES

189 transmission spectra were obtained in the stack scan mode with 0.1-eV resolution across the

190 near edge region and 0.5-eV resolution below and above the near edge absorption. Energy

191 calibration was conducted by measuring CO_2 and N_2 gas prior to the measurements. The

192 absorption spectra (optical density, OD) were obtained as OD = -ln(I/I_0), where I is X-ray
193 intensity transmitted from sample and I_0 is that recorded without samples. Leinweber et al.
194 (2007) and Cody et al. (2008) were referred for the absorption peak assignment.
195 The FIB section was observed under a polarized microscope to check the textural
196 relationships between the MM and the epoxy resin in the section. The section was further
197 observed with a JEOL JEM-2100F field emission TEM, equipped with JEOL JED SDD EDS
198 for detailed textural observation and elemental analysis, at JEOL Corporation and with a
199 JEOL JEM-2100, equipped with an Oxford INCA SDD EDS, at Ibaraki University.
200
201 **3. Results**
202 **3-1. Texture and mineralogy**
203 Figure 1a shows a secondary electron image of an UCAMM D05IB80, which is about ~40
204 x 30 μm in size. There are abundant sub-μm-sized constituents on the surface of the upper
205 half of this UCAMM. By contrast, the other half is poor in the sub-μm-constituents and has a
206 smooth surface. Ultramicrotomed sections of the UCAMM are shown in Fig. 1b. The sections
207 were selected out of every 3-5 serial sections. There are many mineral grains in the sections
208 No. 1 and 2 (Fig. 1b), which may correspond to the sections of the upper half of the UCAMM

209 shown in Fig. 1a. There are voids in each section, which is composed of densely packed
210 hollow organic material with ~0.5- to ~2-μm thick walls containing minerals.

211 TEM observation shows that this UCAMM contains glass with embedded metal and
212 sulfide (GEMS) (Figs. 2a, 2b), which is common to the chondritic porous (CS) IDPs (e.g.
213 Bradley and Dai, 2004), UCAMMs previously investigated (Nakamura et al., 2005; Duprat et
214 al., 2010; Dobrică et al., 2012), and CS MMs (Noguchi et al., 2015). Their typical size ranges
215 from ~200 to ~400 nm in diameter and contains tiny (< 30 nm) Fe sulfide as well as rare Fe
216 metal, which appear as S and Fe enriched spots in the elemental distribution maps (Fig. 2c).
217 Oxygen, aluminum, and silicon are homogeneously distributed and magnesium is
218 heterogeneously distributed in the glassy (amorphous silicate) matrix of this GEMS grain (Fig.
219 2c).

220 Olivine, low-Ca pyroxene, high-Ca pyroxene, amorphous silica, and pyrrhotite are major
221 inorganic phases in this UCAMM (Figs. 2d-2i), and low-Ca pyroxene and pyrrhotite are more
222 abundant than the other phases. Among these phases, amorphous silica containing no other
223 elements is not common in CP IDPs (e.g. Bradley and Dai, 2004), CP MMs (e. g. Noguchi et
224 al., 2015), and UCAMMs investigated previously (Dobrică et al., 2012). No hydrated silicate
225 was found in the UCAMM.

226 Major element compositions of olivine, pyroxene, and pyrrhotite in the UCAMM
227 D05IB80 are shown in Fig. 3 and Table 1. Majority of the GEMS grains in this UCAMM are
228 highly depleted in Mg relative to [Si+Al] and Fe and are plotted at the Mg-poor end of the
229 GEMS grains in CP IDPs (Fig. 3a). In addition, sulfur is also depleted in the GEMS grains
230 (Fig. 3b). These data strongly suggest that GEMS grains in this MM do not keep their original
231 chemical compositions.

232 Olivine is minor in this MM, and the forsterite mol% ranges from ~100 to 89 (Fig. 3c).
233 Low-Ca pyroxene shows a variation of enstatite mol% from ~100 to 78 (Fig. 3c). Because all
234 the high-Ca pyroxene grains analyzed contain high Al_2O_3 contents from 14.7 to 27.8 wt%,
235 they are plotted around the Di apex or outside the pyroxene quadrilateral due to the relative
236 deficiency of Mg^{2+} and Fe^{2+} caused by substitution of Al^{3+} in high-Ca pyroxene (Fig. 3c). FeO
237 vs MnO and FeO vs Cr_2O_3 wt% diagrams show that some low-Ca pyroxene crystals have high
238 MnO (up to 1.85wt%) and high Cr_2O_3 (up to 2.32wt%) contents relative to FeO contents (Figs.
239 3e, f). Most pyrrhotite crystals are poor in Ni. Only two crystals have 2.8 and 3.2 Ni atomic%
240 (Fig. 3d). These data are consistent with the chemical compositions of olivine, pyroxene, and
241 pyrrhotite in CP IDPs, previously reported UCAMMs, and mineral grains recovered from
242 81P/Wild 2 (Klöck and Stadermann, 1994; Zolensky and Barrett, 1994; Zolensky et al., 2006,

2008; Joswiak et al., 2009, 2012; Dobrică et al., 2012; Frank et al., 2014).

3-2. Organic material: size, texture, molecular and isotopic compositions

Size

Figure 4 shows the isotopograph of $^{12}C^{14}N^-$, $^{32}S^-$, and $^{16}O^-$ along with the backscattered electron (BSE) image of the UCAMM D05IB80. The distribution of $^{12}C^{14}N^-$ indicates the size of organic carbon is ~ 15 μm × 15 μm. In comparison to the typical size of organic carbon in chondritic meteorites (a few hundreds nm) (e.g., Le Guillou et al., 2014) and that of comet Wild 2 dust particles (~ 1 - 2 μm) (Cody et al. 2008), the organics in the present study is extraordinarily large. $^{32}S^-$ and $^{16}O^-$ are concentrated in the rim of the organic material (Fig. 4), and $^{32}S^-$ is also distributed within the organic material, although its abundance is less than that in the rim.

Observation of soluble organics

UCAMM D05IB80 was originally almost opaque under a transmitted light, though a translucent brown-color part seeped from the sample when it was embedded in epoxy (Fig. 5b). A certain degree of affinity between the UCAMM and epoxy seems to have taken place,

260 which is shown by the observation that the boundary between the embedding epoxy (light
261 brown) and the UCAMM (dark brown) is less clear in the transmitted optical image (Fig. 5d)
262 than in the high-angle annular dark-field scanning transmission electron microscopy
263 (HAADF-STEM) image (Fig. 5e).
264
265 ***Molecular compositions***
266 A Raman spectrum of carbonaceous material in UCAMM D05IB80 is shown in Fig. 6.
267 The spectrum is broad, and the centers and full width at half maximum (FWHM) of D_1 and G
268 are 1338 cm^{-1} (ω_{D1}) and 369 cm^{-1} (Γ_{D1}), and 1569 cm^{-1} (ω_G) and 109 cm^{-1} (Γ_G), respectively.
269 Although the analytical conditions were different from those of the other studies which
270 investigated CP IDPs, MMs, and carbonaceous chondrites (e.g., Rotundi et al., 2008;
271 Busemann et al., 2009; Dobrică et al. 2011; Dartois et al. 2013), the peak broadness and the
272 wave parameters indicate that the carbonaceous material is very disordered.
273 Combining carbon- and nitrogen-XANES maps of the FIB section, we can distinguish the
274 organic nitrogen-rich regions of the UCAMM from the epoxy that does not contain N (Fig. 7a,
275 b). Nitrogen-XANES spectra of N-rich regions 1 and 2 (Fig. 7d) exhibit intense peaks of
276 1s-π* transitions of imine (C=N*) at 398.8 eV (peak E), aromatic nitrogen heterocycles

277 (C-N*=C) and/or nitrile (C≡N*) at 399.7 eV (peak F), and amide (N*Hx(C=O)C) at ~401.5
278 eV (peak G). The N-XANES spectra provided a sufficient signal- to-noise (S/N) ratio, which
279 has not been generally observed in chondritic insoluble organic matter and even in organic
280 matter in IDPs (Cody et al. 2011). The relative peak intensity of nitrogen heterocycles in the
281 region 2 is higher than that in the region 1. The nitrogen speciation helps the characterization
282 of carbon functional groups in C-XANES spectra (Fig. 7c). The peak A at ~ 285 eV is
283 assigned to 1s-π* transitions of aromatic/unsaturated carbon (C=C*), which probably includes
284 aromatic nitrogen heterocycles (e.g., pyridine) in the regions 1 and 2, due to the presence of
285 imine in their N-XANES. The peak B at ~286.6 eV are derived from 1s-π* transitions of
286 nitrile/aromatic N or vinyl-keto carbon. The presence of nitrile/aromatic N is very likely
287 because of the intense peaks (peak G) in N-XANES of the regions 1 and 2, while the same
288 peak in the epoxy region would be assigned to vinyl-keto group due to the absence of N. A
289 broad peak ranging 287-288 eV for the regions 1 and 2 includes a peak of 1s-3p/ σ *
290 transition to aliphatic carbon (peak C) and a peak D at ~288.3 eV assigned to 1s-π*
291 transitions of carboxyl carbon (C*=O) and/or amidyl carbon (NHx(C*=O)C). The N/C ratio is
292 calculated from the spectral fitting using the aXis 2000 software to be 0.15±0.03, and the O/C
293 ratio is 0.27±0.02, for the region 1. There is a possibility that the XANES results in the

294 present work may be affected by FIB-induced damage, such as an increase of the aromatic
295 carbon (De Gregorio et al. 2010; Bassim et al. 2012). In that case, an original peak intensity
296 of imine may have been relatively lower and those of nitrile and carboxyl groups may have
297 been higher than the acquired spectra. Nevertheless, the possible modification of functional
298 group compositions by FIB should not affect the elemental ratios. Sulfur-XANES
299 measurement was carried out at the BL 5.3.2.1. with a photon energy range of 600-2000 eV,
300 ALS, but the sulfur abundance in the FIB section was below the detection limit of XANES.
301
302 ***Texture***
303 TEM observation of the organic N-rich material reveals the presence of two N-rich
304 regions: the region 1 is smooth and the region 2 is entirely globular (Fig. 8). The two regions
305 are connected at the bottom-left corner of the FIB section (Fig. 5e), indicating that these
306 regions were made of the same organic material as shown in the similar C- and N-XANES
307 spectra (Fig. 7c, d). The globules in the region 2 look similar in size (a few hundred nm) to
308 the organic nanoglobules ubiquitously observed in chondritic meteorites (e.g., Nakamura et al.
309 2002; Garvie and Buseck, 2004; Nakamura-Messenger et al. 2006; Peeters et al. 2012; De
310 Gregorio et al. 2013; Matsumoto et al. 2013), micrometeorites (Sakamoto et al, 2010), IDPs

311 (Busemann et al. 2009) and the comet Wild 2 dust particles (De Gregorio et al. 2010; 2011).
312 However, the organic nanoglobules in UCAMM D05IB80, forming aggregates, have more
313 irregular shapes compared to rounded globules in most carbonaceous chondrites. The
314 nanoglobules appear to contain fillings in their interiors (Fig. 8b, c). The high resolution TEM
315 image of the globule filling is shown in Fig. 9(c), which is an aggregate of tiny crystals.
316 Although EDS spectrum of the aggregate suggests that it is composed of low-Ca pyroxene, it
317 was impossible to determine the phase of the crystals due to their small sizes.
318 TEM images (Fig. 8b, c) revealed that the globular region has three very thin (< 5 nm)
319 surface layers and the smooth region has two (Fig. 8d, e), and the surface layer is less
320 electron-transparent than the interior. The less electron-transparent material is estimated to be
321 amorphous due to the absence of lattice fringes, and is rich in C, O, Si, S, and Fe (Fig. 9),
322 suggesting the presence of silicate and sulfide. High resolution TEM image of the thin layer
323 in the globular region revealed that the layers contain nanocrystals. Although 0.24 and 0.28
324 nm lattice fringes were observed (Fig. 8f), we could not obtain diffraction spots in the
325 selected area electron diffraction (SAED) patterns, which only gave halo patterns. This is
326 probably due to the minute volumes of these nanocrystals. Therefore, we could not identify
327 phases of these nanocrystals. By contrast, we could not find any nanocrystals at the smooth

328 boundaries (Fig. 8g). The thin layers are thought to be indigenous, and are neither reaction
329 products with epoxy resin nor reaction products with filtrated water in the Antarctica, because
330 the layers is specifically present only in the present UCAMM. If the layers were the
331 secondary products on the Antarctic snow, similar layers should be found in other
332 micrometeorites. The layers are also distinct from a magnetite rim at the surface of
333 micrometeorites formed during heating by atmospheric entry and oxidation (Toppani et al.,
334 2001).

335 Sodium, K, and Cl are uniformly observed in the smooth region and sporadically in the
336 globular region (Fig. 9). Halite was also identified by XRD (see electronic supplementary
337 data, S2). Although it is difficult to evaluate whether they are indigenous or terrestrial
338 contamination, the homogeneous distributions of these elements as well as N and S do not
339 look like crystal particles of sea salts. The globular region contains a grain consisting of O,
340 Mg, and Si (Fig. 9b). High resolution TEM image of the grain shows that the grain is a
341 polycrystalline aggregate of tiny crystals. 0.46- and 0.24- nm lattice fringes could be assigned
342 as lattice spacing of (200) (~0.46 nm) and (002) (~0.25 nm) of clinoenstatite by considering O,
343 Mg, and Si are major elements (Fig. 9c).

344

345 ***Isotopic compositions***

346 We found no isotopic hot spots in the organic matter in the UCAMMs (Fig. 10). The H, C
347 and N isotopic ratios of the UCAMM D05IB80 are in the range of terrestrial values and not
348 clearly distinguished from those of epoxy ($<2\sigma_{OM}+3\sigma_{epoxy}$). We conclude that the H, C and N
349 isotopic compositions are at the same level as those of terrestrial organics (Fig. 10).

350

351 **4. Discussion**

352 **4-1. Primitive Nature of UCAMM Organics**

353 The highly resolved N-XANES spectra of UCAMM D05IB80 are significantly different
354 from the less characteristic, low signal-to-noise N-XANES spectra of insoluble organic
355 macromolecules (IOM) from chondritic organic materials (e.g., Cody et al., 2008).
356 According to the spectral fitting, the ratio of nitrogen to carbon in the smooth region of the
357 UCAMM organics (N/C = ~0.15) is five times higher than that of insoluble organic
358 macromolecules in types 1 and 2 chondritic meteorites (N/C = ~0.03, Alexander et al. 2007)
359 (Fig. 11). The high nitrogen abundance and most of the identified functional groups (imine
360 C=N, aromatic nitrogen heterocycles C-N=C, nitrile C≡N, amide NHx(C=O)C, and
361 carbonyls COOR) indicate that the UCAMM organic material has high polarity, which

362 indicates its hydrophilic nature and is consistent with the fact that the organic soluble phase
363 was dissolved into epoxy (*i.e.*, polar solvent) (Fig. 5).

364 In prebiotic organic chemistry, *any* materials become insoluble, tar-like, hydrophobic
365 macromolecules when energy is continuously provided to molecules (Benner et al. 2012).
366 Considering this general chemical phenomema, the nitrogen- and oxygen-bearing polar
367 functional group compositions and the solvent solubility indicate that the UCAMM organic
368 material is extremely primitive compared to those in carbonaceous chondrites.

369

370 **4-2. Formation of UCAMM Organics and the Role of Small Degree of Aqueous**
371 **Alteration**

372 Nitrogen-rich and oxygen-bearing complex organic molecules were synthesized by UV
373 photolysis of ices with simulated interstellar/precometary compositions (e.g., H_2O, CH_3OH,
374 CO, NH_3) (e.g., Bernstein et al. 1995; Dworkin et al. 2001; Nuevo et al. 2011), and they were
375 mostly soluble and/or oily (Bernstein et al. 1995; Dworkin et al. 2001; Nuevo et al. 2011)
376 having nanoglobule-like vesicles (Dworkin et al. 2001). The UCAMM in this study shares a
377 chemical similarity to the synthesized organics; UCAMM contains functional groups of nitrile,
378 imine, and amide (Fig. 7d), which were also observed in the photochemical product by Nuevo

379 et al. (2011). The photochemical reaction of ices in the interstellar or pre-stellar environments
380 may have played a role in forming the organic macromolecules in the UCAMM, but the
381 XANES spectrum of the experimentally synthesized organic matter is not completely the
382 same as the present UCAMM. Furthermore, the bulk N/C (= 0.28) and O/C (= 0.51) ratios of
383 the synthesized materials (Nuevo et al. 2011) are much higher than those of the UCAMM.
384 Therefore, photochemistry alone would not be the process responsible for the formation of
385 UCAMM and an additional process(es) would be necessary.

386 Here we propose that very weak aqueous alteration in the parent body of the UCAMM
387 was responsible for the chemical, structural, mineralogical and morphological characteristics
388 of the UCAMM. Accretion of the organics, ice, submicron-sized mineral particles is a
389 necessary process for forming a certain size of cometary body to retain liquid water, i.e., a
390 meter to kilometer-sized object. In a comet, short-term heating such as planetesimal shock
391 could have locally melted ice grains and released water, which dissolved organic material.
392 Unlike meteorite parent bodies where aqueous fluid mobilizes due to high thermal
393 conductivity with compact mineral structure, it is improbable that aqueous fluid mobilizes in
394 a comet parent body due to very low thermal conductivity of the porous ice structure (40-80%
395 in average) (e.g., Kouchi et al. 1992; Asphaug and Benz, 1996; Farnham and Cochran, 2002;

396 Kofman et al. 2015). Accordingly, the aqueous fluid on a porous icy body allowed formation
397 of a large sized organic puddle.

398 Very low degree of melting of ice in a comet or an icy planetesimal causing low
399 mobilization of the fluid well explains the following observations in the present study;

400 *i) Sulfurization of organics*. UCAMM D05IB80 contains a considerable amount of
401 sulfur, of which source is easily explained if it was formed in a comet or an icy body. H_2S is a
402 typical component of cometary volatiles (Bockelee-Morvan et al., 2004) and also an aqueous
403 alteration product of sulfide. Thus, the icy parent body of UCAMM D05IB80 may have
404 contained it. Nucleophilic attack of H_2S could have taken place on the partially positive
405 carbonyl carbon of the UCAMM organics (Fig. 7c) and/or their precursor molecule in
406 aqueous fluid. For instance, ketones and aldehydes experimentally gave high yields of organic
407 sulfides (R-S_x-R') via a reaction with reduced inorganic sulfur (e.g., HS^-) in aqueous solution
408 at relatively low temperature (20-50°C) for short-duration (e.g., 22 hrs to 4 weeks) (Schouten
409 et al., 1994; van Dongen et al., 2003).

410 *ii) Formation of inorganic nanolayers at the surface of organic material*. The organics
411 in UCAMM D05IB80 is covered with a thin inorganic layer as shown in Fig. 8, which can be
412 explained by the adsorption of mineral nanoparticles to an ice-fluid interface. When a fluid

was frozen, the partition imbalance of anions and cations between ice and liquid occurs, which is relaxed by the transfer of H^+ and OH^- to each phase, resulting in disproportionate pH between the two phases (Watanabe et al. 2014). The ion-transfer current changes at the interface between organics and salt-bearing ice (Qu et al. 2015). At the interface of two phases with strong contrast of pH and redox-potential, silicate and sulfide membranes osmotically precipitate from the dissolved ions in a fluid (Cairns-Smith, 1982; Russel et al. 1994). The interaction of particles at the ice-fluid interface occurs instantaneously at a cooling rate of -10 ~ -15 K/min from room temperature (Körber et al. 1985). The organic nanoglobules in Tagish Lake meteorite displays similar layers that contain predominantly carbon with minor amounts of O, Si, S, Cl and Fe (Nakamura et al. 2002), which may be also because of the behaviors of ions and mineral particles in a frozen aqueous environment of its parent body.

iii) Formation of irregular-shaped nanoglobule aggregates. The organics in UCAMM D05IB80 shows different textures (smooth and globular textures) (Fig. 8), but their similar chemical compositions suggest simultaneous formation from a common precursor material (Fig. 7). The organic nanoglobules, which would have been originally round, deformed their shapes (e.g., budding) via pH gradient and/or change of osmotic pressure by the generation of

430 the small amount of fluid. For instance, the charge state of an organic molecule changes under
431 different pH, such as a protonated carboxylic acid (R-COOH) at lower pH and an ionized
432 carboxylate ($R\text{-}COO^-$) at higher pH. Vesicles are produced around at neutral pH where the
433 molar ratio of the protonated and ionized forms is equal (e.g., Nawa et al. 2013). However,
434 the fluid in a cometary body could have been basic because of the redistributions of ions
435 (Watanabe et al. 2014) and/or high concentration of NH_3 (Nakamura-Messenger et al. 2011).
436 At the high pH, the vesicles are rapidly deformed (in several seconds) due to dissolution of an
437 ionized form (Nawa et al. 2013). Similarly, textural variations of nanoglobules in insoluble
438 organic residues (De Gregorio et al. 2013; Changela et al. 2013) and matrices (Ivuna, Orgueil
439 and Tagish Lake, see electronic supplementary data, S3) from the aqueous altered
440 carbonaceous chondrites imply the exposure to basic fluid that were generated through the
441 formation of phyllosilicates during the aqueous alteration on their meteorite parent bodies.
442
443 **4-3. Mineralogical Evidence of Small Degree of Aqueous Alteration**
444 Although GEMS grains in D05IB80 contain Fe-Ni metal and Fe sulfide tiny crystals (Fig.
445 2), they are rarer than those in GEMS in CP IDPs (e. g. Keller and Messenger, 2011) and CP
446 MMs (Noguchi et al. 2015). Mg in the amorphous silicate in GEMS grains are

447 heterogeneously distributed and on average highly depleted (Fig. 2c). By contrast, Si is
448 enriched in the Mg-depleted areas in GEMS (Fig. 2c). Heterogeneous distribution of Si and
449 Mg within each GEMS grain in IDPs has already been reported (e.g., Keller and Messenger,
450 2011). In the case of D05IB80, Si-rich areas are predominant and amorphous silicate is
451 enriched in Fe (Figs. 2, 3).

452 Because Fe-Ni metal is among the first phase to alter by aqueous alteration (Zolensky et al.
453 1993; Hanowski and Brearley 2000, 2001; Chizmadia et al. 2008), the rarity of nano Fe metal
454 in GEMS indicates a slight degree of aqueous alteration. It has been already reported that rare
455 Fe-Ni metal phases were found from the UCAMMs and their GEMS-like objects collected by
456 the French-Italian team (Dobrică et al. 2012). The depletion of metal may be a common
457 feature of UCAMMs. The GEMS grains with rare nanophase Fe metal particles in the Acfer
458 094 carbonaceous chondrite (Vollmer et al., 2009a, b) have been thought to be the results of
459 oxidation of Fe metal due to nascent aqueous alteration of the amorphous silicates (Keller et
460 al. 2009). Le Guillou and Brearley (2014) reported the absence of metal grains associated
461 with the amorphous silicate material in MET 00426 CR3 chondrite, and discussed that the
462 absence was due to hydration of the amorphous silicate.

463 In the case of D05IB80, nano Fe sulfide is also depleted in GEMS. It does not necessarily

464 mean that D05IB80 experienced slightly higher degrees of aqueous alteration than the
465 primitive meteorites because hydrous phyllosilicates are not identified in the UCAMM. A
466 slightly oxidizing condition of aqueous alteration might have promoted dissolution of nano Fe
467 sulfide in GEMS of the UCAMM.

468 There is no Ni-bearing pyrrhotite in the UCAMM (< 3.2 atomic% Ni) (Fig. 3d), which is
469 consistent with the idea that the UCAMM experienced very weak aqueous alteration. The
470 minimal degree of aqueous alteration is also consistent with that aqueous alteration products
471 were not found on olivine and pyroxene (Fig. 6).

472 Based on the chemical and mineralogical features described above, we conclude that the
473 UCAMM experienced a very weak degree of aqueous alteration on a cometary nucleus or an
474 icy asteroid, which are not seen on the typical types 1 and 2 chondritic meteorite parent
475 bodies. Possible heat source for the generation of liquid water in icy small bodies is i)
476 short-lived radioactive nuclides, ii) perihelion passage (Nakamura-Messenger et al. 2011), iii)
477 collisions of planetesimals (Cody et al. 2011), or iv) reduction of the freezing point by the
478 presence of solutes, e.g., ammonia (Pizzarello et al. 2011) and methanol.

479 The condition of aqueous alteration of the UCAMM can be estimated by the experiments
480 by Nakamura-Messenger et al. (2011). They have conducted a hydrothermal experiment of

481 anhydrous IDPs and reported the rapid formation of hydrated silicates at 25-160°C for 12-24
482 hours under basic pH conditions (pH=12), that is, alteration of amorphous silicate into
483 hydrous phyllosilicate possibly proceeds extremely quickly. UCAMM DO05IB80 does not
484 contain hydrous silicates but Mg and S leached out from GEMS grains instead, which
485 indicates a shorter duration reaction at lower temperature, lower pH and/or slightly oxidizing
486 conditions compared to their experiments. Considering that the degree of alteration should
487 have been much lower than aqueous alteration in the major CM and CI carbonaceous
488 chondrites that lasted for several million years (e.g., Fujiya et al. 2013), planetesimals
489 collisions are most likely to produce a very weak degree of aqueous alteration in a short
490 duration. The large $P\Delta V$ irreversible energy deposition during compaction of pore spaces of
491 cometary ices initiates melting at very low shock pressures of 0.1-0.5 GPa between 250 and
492 150K (Stewart and Ahrens, 2004). The pressure range is comparable to the typical impact
493 velocities of comets generating the peak pressures of ~1 GPa (Stewart and Ahrens, 2004).
494 Although there may be a possibility that the UCAMM had suffered terrestrial weathering
495 in Antarctic snow, the possibility would be low because iron hydroxide, which is easily
496 formed by weathering of pyrrhotite (Taylor et al. 2002), is not identified. The residence time
497 of the micrometeorites at the Antarctic snow is much shorter (ca. a year) than the lifetime of

498 the Antarctic ice (ca. thousands years), and the average temperatures near the Dome Fuji
499 station is -54°C (Shiraishi, 2012), which would prevent the weathering reaction.
500
501 **4-4. Comparison with Other UCAMMs, AMMs, IDPs, Comets, and Chondritic**
502 **Meteorites**
503 UCAMM D05IB80 consists of large (tens of micrometers) organic material with
504 submicron-sized mineral species such as crystalline silicate, sulfide, and GEMS grains.
505 Similarly, UCAMMs investigated by Duprat et al. (2010) and Dobrică et al. (2012) have
506 continuous large areas composed of carbonaceous material, and minerals and GEMS grains
507 are embedded in the carbonaceous material. The nitrogen chemical characteristics of organic
508 material in the UCAMM D05IB80 is consistent with those described by Dartois et al. (2013),
509 who identified C=N and C≡N from their non-FIB UCAMM samples. The similarity suggests
510 that the organic chemistry and mineralogy identified in the present study are common for
511 UCAMMs, although GEMS grains in their UCAMMs are enriched in Fe sulfide nanocrystals
512 and do not show depletion of Mg and S.
513 The isotopic compositions of UCAMMs appear to be highly variable; D, ^{13}C, and ^{15}N
514 isotopic compositions are normal in this study, which is also the case for a UCAMM

515 containing abundant presolar grains (Floss et al., 2012). On the contrary, extreme enrichments
516 of D and ^{15}N are found in two UCAMMs by the French-Italian team (Duprat et al. 2010;
517 Dartois et al. 2013). Duprat et al. (2010) showed that one UCAMM had an area of larger D
518 excess ($\delta D > \sim 10000‰$) than another ($\delta D > 5400‰$) with a clear boundary. Indeed, the
519 stratosphere IDPs (Messenger, 2000) and the comet Wild 2 dust particles (Matrajt et al. 2012)
520 show a wide range of the H and N isotopic compositions from values extremely rich in
521 heavy-isotopes to normal values with the terrestrial levels. Thus, it is difficult to determine
522 the origin of the samples only with the presence or absence of the isotopic anomalies.
523 An anhydrous interplanetary dust particle (IDP) L2006LB23 is comprised mainly of
524 carbonaceous material (~90%) (Thomas et al. 1994). The IDP is regarded as an
525 ultracarbonaceous IDP. The ultramicrotomed section (Figs. 1 and 2 in Thomas et al. 1994)
526 has a bubble-wall structure made by organic material containing minerals grains, which is
527 quite similar to the sections of the UCAMM D05IB80. Not only the internal structure, but
528 also mineralogy of the ultracarbonaceous IDP is similar to the UCAMM D05IB80. The IDP
529 contains Si-rich glass containing Fe sulfide and Fe-Ni metal grains, Si-rich glass, pyroxene,
530 olivine, and Fe sulfide. In addition to pyroxene, olivine, and Fe sulfide, the UCAMM
531 D05IB80 contains amorphous SiO_2 and GEMS grains that are highly depleted in Mg and S

532 (Figs. 2, 3). It is likely that these two phases correspond to Si-rich glass and Si-rich glass
533 containing Fe sulfide and Fe-Ni metal grains in L2006LB23. These data suggest that there is a
534 genetic relationship between these objects.

535 Mineralogy and nitrogen-rich organic functional group chemistry were common to the
536 UCAMM D05IB80 and one of the anhydrous AMMs (D10IB009) collected from the
537 Antarctic snow near Dome Fuji station (Noguchi et al. 2017). On the other hand, a difference
538 is that D10IB009 contains GEMS including Fe-metal, and thus it is likely that the UCAMM
539 D05IB80 is aqueously more altered than the anhydrous AMM. Another difference is that the
540 organic material in D10IB009 has D- and ^{15}N-enrichments (δD = ~2000-10000‰, δ^{15}N =
541 ~300-1000‰) (Noguchi et al. 2017), similarly to CP-IDPs (e.g., Messenger et al. 2000),
542 although it is unlikely that the lack of isotopic anomalies in the UCAMM be due to the
543 aqueous alteration, based on the facts that a number of aqueous altered carbonaceous
544 chondrites retain organics enriched in the heavy isotopes (e.g., Busemann et al. 2006;
545 Nakamura-Messenger et al. 2006; Hashiguchi et al. 2013).

546 It should be noted that the N-XANES spectra of the regions 1 and 2 in the UCAMM
547 D05IB80 (Fig. 7d) are very similar to those of three particles of comet Wild 2 with N/C ratios
548 of 0.08-0.16, one of which was an organic nanoglobule with the nitrogen isotopic

549 composition indistinguishable from the terrestrial values (De Gregorio et al., 2010). Other
550 particles of comet Wild 2 have lesser amounts of imine, nitrile, and amidyl groups than amino,
551 urea, and carbamoyl (NHx(C=O)OR) groups in their N-XANES spectra (Cody et al., 2008),
552 but the N/C (~ 0.12) and O/C (0.22 – 0.28) ratios of some of the spectra are comparable to
553 those in this study (Fig. 11). Moreover, the appearance of the organic soluble phase in
554 UCAMM D05IB80 extracted from epoxy (Fig. 5) is similar to those of the epoxy-soluble
555 organic matter in the comet Wild 2 dust particles (Cody et al. 2008; De Gregorio et al. 2011).
556 The chemical and isotopic characteristics of UCAMM-D05IB90 are significantly different
557 from the organic materials in types 1 and 2 carbonaceous chodrites (e.g., Cody et al., 2011),
558 while they are similar to some of the primitive CR3 chondrites. The large smooth organic
559 material connected with globular organics in the UCAMM is similar to that in a CR3
560 chondrite, MET 00426, observed by Le Guillou and Brearley (2014), which is an elongated
561 vein 3–4 μm in length and up to 1 μm width, with a sharp boundary between surrounding
562 silicates and sulfides. They observed a single organic nanoglobule embedded in the main
563 organic mass and an aggregate of rounded particles connected to the main vein. Peeters et al.
564 (2012) also found a several micron-sized organic vein containing a number of nanoglobules in
565 QUE 99177 CR3 chondrite, of which N-XANES spectrum is similar to our observation. The

566 comet Wild 2 is estimated to have experienced little or no aqueous alteration on the basis of
567 the absence of phyllosilicates (Zolensky et al. 2006). CR3 chondrites contain abundance
568 amorphous silicates (e.g., Abreu and Brearley, 2010; Le Guillou and Brearley, 2014) and are
569 thought to have experienced the earliest stage of parent body aqueous alteration. Therefore,
570 the similarities among the organics in the UCAMM D05IB80, the comet Wild 2, and CR3
571 chondrites corroborate that the UCAMM are more primitive than most of the
572 aqueously-altered carbonaceous chondrites.

573 The recent results by the Rosetta mission unveiled the presence of organic-rich, dark
574 dehydrated surface of the comet 67P/Churyumov-Gerasimenko by the Visible, Infrared and
575 Thermal Imaging Spectrometer (VIRTIS) (Capaccioni et al. 2015). The evolved gas analyzer
576 Cometary Sampling and Composition (COSAC) mass spectrometry identified a number of
577 nitrogen-bearing organic molecules, such as nitriles, amines, amides, and isocyanates, but no
578 sulfur species on the comet 67P/C-G (Goesmann et al. 2015). The high abundance and
579 chemical compositions of organics on the comet 67P/Churyumov-Gerasimenko may be
580 related to the precursor material of large N-rich organics of the UCAMM, prior to organic
581 sulfurization under aqueous condition.

582 Moreover, our work reports the first finding of organic materials retaining C, H, O, N and

583 S elements all together from micrometeorites. Another finding of CHONS organics has been
584 reported from the polar solvent extracts from Murchison meteorite (Schmitt-Kopplin et al.
585 2010). Because of the unusual similarity in the organic elemental compositions and polar
586 nature between the UCAMM and Murchison, the possibility that the UCAMM organics
587 contains the precursor of the meteoritic CHONS compounds is expected, and could be a key
588 indicator of the comet-asteroid continuum. In order to trace back and determine the precursors
589 of organic materials in the early Solar System, further analyses and comparative studies of the
590 most primitive extraterrestrial materials we can obtain, such as anhydrous micrometeorites,
591 IDPs and the least altered carbonaceous chondrites through the comprehensive inorganic and
592 organic analytical strategies without discrimination between soluble and insoluble, will be
593 necessary.
594
595 **5. Summary**
596 An ultracarbonaceous micrometeorite (UCAMM D05IB80), collected from near the
597 Dome Fuji Station, Antarctica, has been investigated by coordinated *in-situ* analyses.
598 According to the following unique features of organics and minerals that are different from
599 chondritic meteorites, we conclude that the UCAMM was formed by small amount of

600 fluid-induced interaction of organics and minerals in a porous ice-rich cometary body.

601 1. A major part of the organic materials in the UCAMM shows a smooth texture to which
602 globular aggregates are connected, and includes an epoxy-soluble phase. The UCAMM
603 shows nitrogen-rich organic chemistry (N/C = 0.15). Its organic functional groups include
604 a variety of nitrogen-bearing groups; heterocyclic nitrogen, nitrile, imine, and amide. The
605 polar functional group compositions and the solvent solubility indicate very primitive
606 nature of the organic material in the UCAMM.

607 2. GEMS grains are depleted in Mg and S. This is an evidence for incipient aqueous
608 alteration in the UCAMM parent body. Shock heating in an icy planetesimal
609 instantaneously melted ice grains and released water, which dissolved organic material.
610 Due to the high porosity and low density of a cometary body, the fluid did not diffuse but
611 formed a large-size organic puddle (15 x 15 μm). The locally generated fluid sulfurized
612 organic material, formed mineral thin layers (C, O, Si, S, and Fe) at the surface of
613 organics, and deformed the shape of organic nanoglobules.

614

615 **Acknowledgements**

616 We appreciate Christine Floss, anonymous reviewer, and associate editor Eric Quirico for

617 their constructive comments and helpful editorial handling. This work is supported by a
618 Grant-in-Aid for Scientific Research from the Japanese Ministry of Education, Culture, Sports,
619 Science and Technology (No. 22224010, PI: H. Nagahara). The STXM facility at the
620 beamline 5.3.2.2, ALS, is supported by the Department of Energy, Basic Energy Sciences
621 program.

622

623 **References**

624 Abreu N. M. and Brearley A. J. (2010) Early solar system processes recorded in the matrices
625 of two highly pristine CR3 carbonaceous chondrites, MET 00426 and QUE 99177.
626 *Geochim. Cosmochim. Acta* **74**, 1146– 1171.

627 Alexander C. M. O'D., Fogel M., Yabuta H. and Cody G. D. (2007) The origin and evolution
628 of chondrites recorded in the elemental and isotopic compositions of their
629 macromolecular organic matter. *Geochim. Cosmochim. Acta* **71**, 4380– 4403.

630 Asphaug E. and Benz W. (1996) Size, Density, and Structure of Comet Shoemaker–Levy 9
631 Inferred from the Physics of Tidal Breakup. *Icarus* **121**, 225-248.

632 Bassim N. D., De Gregorio B. T., Kilcoyne A. L. D., Scott K., Chou T., Wirick S., Cody G.
633 and Stroud R. M. (2012) Minimizing damage during FIB sample preparation of

softmaterials. *J. Microscopy* **245**, 288–301.

Benner S. A., Kim, H-J. and Carrigan M.A. (2012) Asphalt, water, and prebiotic synthesis of ribose, ribonucleosides, and RNA. *Acc. Chem. Res.* **45**, 2025-2034.

Bernstein M. P., Sandford S. A., Allamandola L. J., Chang S. and Scharberg M. A. (1995) Organic Compounds Produced by Photolysis of Realistic Interstellar and Cometary Ice Analogs Containing Methanol. *Astrophys. J.* **454**, 327–344.

Bockelée-Morvan D., Crovisier J., Mumma M. J., and Weaver H. A. (2004) The composition of cometary volatiles. In Comets II (eds. Festou M. C., Keller H. U., and Weaver H. A.) Tucson, AZ: The University of Arizona Press. pp. 391–423.

Bradley J. P. and Brownlee D. E. (1986) Cometary particles: Thin sectioning and electron beam analysis. *Science* **231**, 1542-1544.

Bradley J. P. and Dai Z. R. (2004) Mechanism of formation of glass with embedded metal and sulfides. *The Astrophysical Journal* **617**, 650-655.

Bradley J. P., Keller L. P., Snow T. P., Hanner M. S., Flynn G. J., Gezo J. C., Clemett S. J., Brownlee D. E. and Bowey J. E. (1999) An infrared spectral match between GEMS and interstellar grains. *Science* **285**, 1716-1718.

Busemann H., Young A. F., Alexander C. M. O'D., Hoppe P., Mukhopadhyay S. and Nittler

651 L. R. (2006) Interstellar chemistry recorded in organic matter from primitive meteorites.
652 *Science* **314**, 727–730.
653 Busemann H., Nguyen A. N., Cody G. D., Hoppe, P., Kiloyne, A. L. D., Stroud, R. M., Zega
654 T. J. and Nittler L. R. (2009) Ultra-primitive interplanetary dust particles from the comet
655 26P/Grigg–Skjellerup dust stream collection. *Earth Planet. Sci. Lett.* **288**, 44–57.
656 Cairns-Smith A. G (1982) Genetic takeover and the mineral origins of life. Cambridge
657 University Press, Cambridge, England.
658 Capaccioni, F., Coradini, A., Filacchione, G., et al. (2015) *Science* **349**, aab0628-1-
659 aab0628-4.
660 Changela H. G., Cody G. D., Alexander C. M. O'D., Nittler L. R., Peeters Z., De Gregorio B.
661 T. and Stroud R. M. (2013) TEM Study of insoluble organic matter in primitive
662 chondrites: Unusual textures associated with organic nanoglobules. *Lunar Planet. Sci.*
663 **XLIV**, #3101.
664 Chizmadia L. J., Xu Y., Schwappach C. and Brearley A. J. (2008) Characterization of
665 micron-sized Fe,Ni metal grains in fine-grained rims in the Y-791198 CM2 carbonaceous
666 chondrite: Implications for asteroidal and preaccretionary models for aqueous alteration.
667 *Meteor. Planet. Sci.* **43**, 1419–1438.

668 Cody G. D., Ade H., Alexander C. M. O'D., Araki T., Butterworth A., Fleckenstein H., Flynn
669 G., Gilles M. K., Jacobsen C., Kilcoyne A. L. D., Messenger K., Sandford S. A.,
670 Tyliszczak T., Westphal A. J., Wirick S. and Yabuta H. (2008) Quantitative organic and
671 light-element analysis of comet 81P/Wild 2 particles using C-, N-, and O- XANES.
672 *Meteor. Planet. Sci.* **43**, 353–365.
673 Cody G. D., Heying E., Alexander C. M. O. D., Nittler L. R., Kilcoyne A. L. D., Sandford S.
674 A. and Stroud R. M. (2011) Establishing a molecular relationship between chondritic and
675 cometary organic solids. *Proc. Natl. Acad. Sci. USA* **108**, 19171–19176.
676 Dartois E., Engrand C., Brunetto R., Duprat J., Pino T., Quirico E., Remusat L., Bardin N.,
677 Briani G., Mostefaoui S., Morinaud G., Crane B., Szwec N., Delauche L., Jamme F.,
678 Sandt Ch. and Dumas P. (2013) Ultracarbonaceous Antarctic micrometeorites, probing
679 the Solar System beyond the nitrogen snow-line. *Icarus* **224**, 243–252.
680 De Gregorio B. T., Stroud R. M., Nittler L. R., Alexander C. M.O'D., Kilcoyne A. L. D. and
681 Zega T. J. (2010) Isotopic anomalies in organic nanoglobules from Comet 81P/Wild 2:
682 Comparison to Murchison nanoglobules and isotopic anomalies induced in terrestrial
683 organics by electron irradiation. *Geochim. Cosmochim. Acta* **74**, 4454-4470.
684 De Gregorio B. T., Stroud R. M., Cody G. D., Nittler L. R., Kilcoyne A. L. D. and Wirick S.

685 (2011) Correlated microanalysis of cometary organic grains returned by Stardust. *Meteor*.
686 *Planet*. *Sci*. **46**, 1376-1396.
687 De Gregorio B. T., Stroud R. M., Nittler L. R., Alexander C. M.O'D., Bassim N. D., Cody G.
688 D., Kilcoyne A. L. D., Sandford S. A., Milam S. N., Nuevo M. and Zega T. J. (2013)
689 Isotopic and chemical variation of organic naoglobules in primitive meteorites. *Meteor*.
690 *Planet*. *Sci*. **48**, 904-928.
691 Dobricaˇ E., Engrand C., Quirico E., Montagnac G. and Duprat J. (2011) Raman
692 characterization of carbonaceous matter in CONCORDIA Antarctic micrometeorites.
693 *Meteor*. *Planet*. *Sci*. **46**, 1363-1375.
694 Dobricaˇ E., Engrand C., Leroux H., Rouzaud J.-N. and Duprat J. (2012) Transmission
695 electron microscopy of CONCORDIA ultracarbonaceous Antarctic micrometeorites
696 (UCAMMs): Mineralogical properties. *Geochim*. *Cosmochim*. *Acta* **76**, 68–82.
697 Duprat J., Dobrica E., Engrand C., Aléon J., Marrocchi Y., Mostefaoui, S., Meibom A.,
698 Leroux H., Rouzaud J.-N., Gounelle M., Robert F. (2010) Extreme deuterium excesses in
699 ultracarbonaceous micrometeorites from central Antarctic snow. *Science* **328**, 742-745.
700 Dworkin J. P., Deamer D. W., Sandford S. A. and Allamandola L. J. (2001) Self-assembling
701 amphiphilic molecules: Synthesis in simulated interstellar/precometary ices. *Proc*. *Natl*.

Acad. Sci. USA **98**, 815-819.

Farnham T. L. and Cochran A. L. (2002) A McDonald Observatory Study of Comet 19P/Borrelly: Placing the Deep Space 1 Observations into a Broader Context. *Icarus* **160**, 398-418.

Floss C., Noguchi T. and Yada T. (2012) Ultracarbonaceous Antarctic micrometeorites: Origins and relationships to other primitive extraterrestrial materials. *Lunar Planet. Sci.* **XLIII**, #1217.

Floss C., Stadermann F. J., Bradley J., Dai Z. R., Bajt S., and Graham G. (2004) Carbon and nitrogen isotopic anomalies in an anhydrous interplanetary dust particle. *Science* **303**, 1355-1358.

Frank D. R., Zolensky M. E. and Le L. (2014) Olivine in terminal particles of Stardust aerogel tracks and analogous grains in chondrite matrix. *Geochim. Cosmochim. Acta* **142**, 240–259.

Fujiya W., Sugiura N., Sano Y. and Hiyagon H. (2013) Mn–Cr ages of dolomites in CI chondrites and the Tagish Lake ungrouped carbonaceous chondrite. *Earth Planet. Sci. Lett.* **362**, 130–142.

Garvie L. A. J. and Buseck P. R. (2004) Nanosized carbon-rich grains in carbonaceous

719 chondrite meteorites. *Earth Planet. Sci. Lett.* **224**, 431–439.

720 Goesmann F., Rosenbauer H., Bredehoft J. H., Cabane M., Ehrenfreund P., Gautier T., Giri
721 Chaitanya, Kruger H., Le Roy L., MacDermott A. J., McKenna-Lawlor S., Meierhenrich
722 U. J., Munoz Caro G. M., Raulin F., Roll R., Steele A. Steininger H., Sternberg R., Szopa
723 C., Thiemann W. and Ulamec S. (2015) Organic compounds on comet
724 67P/Churyumov-Gerasimenko revealed by COSAC mass spectrometry. *Science* **349**,
725 aab0689-1- aab0689-3.

726 Greenberg J. M. and Li A. (1997) Silicate core-organic refractory mantle particles as
727 interstellar dust and as aggregated in comets and stellar disks. *Adv. Space Res.* **19**, 981–
728 990.

729 Hanowski N. P. and Brearley A. J. (2000) Iron-rich aureoles in the CM carbonaceous
730 chondrites, Murray, Murchison and ALH81002: Evidence for in situ alteration. *Meteor.*
731 *Planet. Sci.* **35**, 1291–1308.

732 Hanowski N. P. and Brearley A. J. (2001) Aqueous alteration of chondrules in the CM
733 carbonaceous chondrites, Allan Hills 81002. *Geochim. Cosmochim. Acta* **65**, 495–518.

734 Hashiguchi M., Kobayashi S. ad Yurimoto H. (2013) In situ observation of D-rich
735 carbonaceous globules embedded in NWA 801 CR2 chondrite. *Geochim. Cosmochim.*

736 *Acta* **122**, 306-323.

737 Joswiak D. J., Brownlee D. E., Matrajt G., Westphal A. J. and Snead C. J. (2009)
738 Kosmochloric Ca-rich pyroxenes and FeO rich olivines (Kool grains) and associated
739 phases in Stardust tracks and chondritic porous interplanetary dust particles: possible
740 precursors to FeO-rich type II chondrules in ordinary chondrites. *Meteorit. Planet. Sci.* **44**,
741 1561–1588.

742 Joswiak D. J., Brownlee D. E., Matrajt G., Westphal A. J., Snead C. J. and Gainsforth Z.
743 (2012) Comprehensive examination of large mineral and rock fragments in Stardust
744 tracks: mineralogy, analogous extraterrestrial materials, and source regions. *Meteorit.*
745 *Planet. Sci.* **47**, 471–524.

746 Keller L. P. and Messenger S. (2011) On the origins of GEMS grains. *Geochim. Cosmochim.*
747 *Acta* **75**, 5336–5365.

748 Keller L. P., Nakamura-Messenger K. and Messenger S. (2009) Amorphous silicates in
749 primitive meteoritic materials: Acfer 094 and IDPs. 72nd Annual Meteoritical Society
750 Meeting 44. #5371 (abstract).

751 Kilcoyne A. L. D., Tyliszczak T., Steele W. F., Fakra S., Hitchcock P., Franck K., Anderson
752 E., Harteneck B., Rightor E. G., Mitchell G. E., Hitchcock A. P., Yang L.,Warick T. and

753 Ade, H. (2003) Interferometer controlled scanning transmission microscopes at the
754 Advanced Light Source. *J. Synchrotron Rad.* **10**, 125–136.
755 Klöck W. and Stadermann F. J. (1994) Mineralogical and chemical relationships of
756 interplanetary dust particles, micrometeorites and meteorites. In Analysis of
757 Interplanetary Dust (eds. M. E. Zolensky et al.,), pp. 51–87. AIP Conference Proceedings
758 310, New York.
759 Kofman et al. (2015) Properties of the 67P/Churyumov-Gerasimenko interior revealed by
760 CONSERT radar. Science **349**, aab0639-1 – aab0639-6.
761 Körber C., Rau G., Cosman M. D. and Cravalho E. G. (1985) Interaction of particles and a
762 moving ice-liquid interface. *J. Cryst Growth* **72**, 649-662.
763 Kouchi A., Greenberg J. M., Yamamoto T., and Mukai T. (1992) Extremely low thermal
764 conductivity of amorphous ice: relevance to comet evolution. *Astrophys. J.* **388**,
765 L73-L76.
766 Le Guillou C. and Brearley, A. J. (2014) Relationships between organics, water and early
767 stages of aqueous alteration in the pristine CR3.0 chondrite MET00426. *Geochim.*
768 *Cosmochim. Acta*, **131**, 344-367.
769 Le Guillou C., Bernard S., Brearley, A. J. and Remusat L. (2014) Evolution of organic matter

770 in Orgueil, Murchison and Renazzo during parent body aqueous alteration: *In situ*
771 investigations. *Geochim. Cosmochim. Acta*, **131**, 368-392.
772 Leinweber P., Kruse J., Walley F. L., Gillespie A., Eckhardt K-U., Blyth R. I. R. and Regier T.
773 (2007) Nitrogen K-edge XANES – an overview of reference compounds used to identify
774 'unknown' organic nitrogen in environmental samples. *J. Synchrotron Rad.* **14**, 500–511.
775 Matrajt G., Messenger S., Brownlee D. and Joswiaki D. (2012) Diverse forms of primordial
776 organic matter identified in interplanetary dust particles. *Meteor. Planet. Sci.* **47**,
777 525-549.
778 Matsumoto T., Tsuchiyama, A., Nakamura-Messenger, K., Nakano, T., Uesugi, K., Takeuchi,
779 A. and Zolensky, M. E. (2013) Three-dimensional observation and morphological
780 analysis of organic nanoglobules in a carbonaceous chondrite using X-ray
781 micro-tomography. *Geochim. Cosmochim. Acta* **116**, 84-95.
782 Messenger S. (2000) Identification of molecular-cloud material in interplanetary dust particles.
783 *Nature* **404**, 968-971.
784 Messenger, S., Sandford, S. and Brownlee, D. (2006) The population of starting materials
785 available for Solar System construction. *In: Meteorites and the Early Solar System II* (eds.
786 Lauretta D. S. and McSween, H. Y., Jr.) Univ. of Arizona, USA, pp. 187-208.

787 Nakamura K., Zolensky M. E., Tomita S., Nakashima S. and Tomeoka K. (2002) Hollow
788 organic globules in the Tagish Lake meteorite as possible products of primitive organic
789 reactions. *International Journal of Astrobiology* **1**, 179-189.
790 Nakamura T., Noguchi T., Ozono Y., Osawa T. and Nagao K. (2005) Mineralogy of
791 ultracarbonaceous large micrometeorites. *Meteor. Planet. Sci.* **40**, A110.
792 Nakamura-Messenger K., Messenger S., Keller L. P., Clemett S. J. and Zolensky M. E.
793 (2006) Organic globules in the Tagish Lake meteorite: remnants of the protosolar disk.
794 *Science* **314**, 1439– 1442.
795 Nakamura-Messenger K., Clemett S. J., Messenger S. and Keller L. P. (2011) Experimental
796 aqueous alteration of cometary dust. *Meteor. Planet. Sci.* **46**, 843–856.
797 Nawa E., Nishigaki Y., Yamamoto D. and Shioi A. (2013) Rhythmic shape change of a
798 vesicle under a pH gradient. *Soft Matter* **9**, 7832-7842.
799 Noguchi T., Ohashi N., Tsujimoto S., Mitsunari T., Bradley J. P., Nakamura T., Toh S.,
800 Stephan T., Iwata N. and Imae N. (2015) Cometary dust in Antarctic ice and snow: Past
801 and present chondritic porous micrometeorites preserved on the Earth's surface. *Earth*
802 *Planet. Sci. Lett.* **410**, 1-11.
803 Noguchi T., Yabuta H., Itoh S., Sakamoto N., Mitsunari T., Okubo A., Okazaki R., Nakamura

804 T., Tachibana S., Terada K., Ebihara M., Imae N., Kimura M. and Nagahara H. (2017)
805 Variation of mineralogy and organic material during the early stages of aqueous activity
806 recorded in Antarctic micrometeorites. *Geochim. Cosmochim. Acta* **208**, 119–144.
807 Nuevo M., Milam S. N., Sandford S. A., De Gregorio B. T., Cody G. D. and Kilcoyne A.L.D.
808 (2011) XANES analysis of organic residues produced from the UV irradiation of
809 astrophysical ice analogs. *Adv. Space Res.* **48**, 1126–1135.
810 Peeters Z., Changela H. G., Stroud R. M., Alexander C. M. O'D. and Nittler L. R. (2012)
811 Coordinated analysis of in situ organic material in the CR chondrite QUE 99177. *Lunar*
812 *Planet. Sci.* **XLIII**, #2612.
813 Pizzarello S. Williams L. B., Lehman J., Holland G. P. and Yarger J. L. (2011) Abundant
814 ammonia in primitive asteroids and the case for a possible exobiology. *Proc. Nat. Acad.*
815 *Sci. USA* **108**, 4303-4306.
816 Qu H., Harada M. and Okada T. (2015) Ion-transfer voltammetry at the interface between
817 organic and salt-doped ice phases. *ChemElectroChem* **2**, 1249-1253.
818 Rotundi A., Baratta G. A., Borg J., Brucato J. R., Busemann H., Colangeli L., d'Hendecourt
819 L., Djouadi Z., Ferrini G., Franchi I. A., Fries M., Grossemy F., Keller L. P., Mennella V.,
820 Nakamura K., Nittler L. R., Palumbo M. E., Sandford S. A., Steele, A. and Wopenka, B.

(2008) Combined micro-Raman, micro-infrared, and field emission scanning electron microscope analyses of comet 81P/Wild 2 particles collected by Stardust. *Meteorit. Planet. Sci.* **43**, 367–397.

Russell M. J., Daniel R. M., Hall A. J. and Sherringham J. A. (1994) A hydrothermally precipitated catalytic iron sulphide membrane as a first step toward life. *J. Mol. Evol.* **39**, 231-243.

Sakamoto K., Nakamura T., Noguchi, T. and Tsuchiyama, A. (2010) A new variant of saponite-rich micrometeorites recovered from recent Antarctic snowfall. *Meteorit. Planet. Sci.* **45**, 220–237.

Schmitt-Kopplin P., Gabelica Z., Gougeon R. D., Fekete A., Kanawati B., Harir M., Gebefuegi I., Eckel G. and Hertkorn N. (2010) High molecular diversity of extraterrestrial organic matter in Murchison meteorite revealed 40 years after its fall. *Proc. Natl. Acad. Sci. USA* **107**, 2763–2768.

Schouten S., de Graaf W., Sinninghe Damsté J. S., van Driel G. B., de Leeuw J. W. (1994) Laboratory simulation of natural sulphurization: II. Reaction of multi-functionalized lipids with inorganic polysulphides at low temperatures. *Org. Geochem.* **22**, 825-834.

Shiraishi K. (2012) Dome fuji station in east antarctica and the Japanese antarctic research

838 expedition. *Proceedings of the International Astronomical Union* **8**, 161-168.

839 Stewart S. T. and Ahrens T. J. (2004) A new H_2O ice Hugoniot: Implications for planetary
840 impact events. *AIP Conf. Proc.* **706**, 1478-1483.

841 Taylor L. A., Nazarov M. A., Shearer C. K., McSween H. Y., Cahill J., Neal C. R., Ivanova
842 M. A., Barsukova L. D., Lentz R. C., Clayton R. N. and Mayeda T. K. (2002) Martian
843 meteorite Dhofar 019: A new shergottite. *Meteor. Planet. Sci.* **37**, 1107–1128.

844 Thomas K., Keller L.P., Blanford G. E. and McKay D. S. (1994) Quantitative analyses of
845 carbon in anhydrous and hydrated interplanetary dust particles. in: Analysis of
846 interplanetary dust, (M. E. Zolensky, T. L. Wilson, F. J. M. Rietmeijer, G. J. Flynn eds),
847 165-172.

848 Toppani A., Libourel G., Engrand C. and Maurette M. (2001) Experimental simulation of
849 atmospheric entry of micrometeorites. *Meteor. Planet. Sci.* **36**, 1377-1396.

850 van Dongen B. E., Schouten S., Baas M., Geenevasen J. A. J. and Sinninghe Damsté J. S.
851 (2003) An experimental study of the low-temperature sulfurization of carbohydrates. *Org.*
852 *Geochem.* **34**, 1129–1144.

853 Vollmer C., Brenker F. E., Hoppe P. and Stroud R. M. (2009a) Direct laboratory analysis of
854 silicate stardust from rRed giant stars. *Astrophys. J.* **700**, 774–780.

855 Vollmer C., Hoppe P., Stadermann F. J., Floss C. and Brenker F. E. (2009b) NanoSIMS
856 analysis and Auger electron spectroscopy of silicate and oxide stardust from the
857 carbonaceous chondrite Acfer 094. *Geochim. Cosmochim. Acta* **73**, 7127–7149.
858 Watanabe H., Otsuka T., Harada M. and Okada T. (2014) Imbalance between anion and
859 cation distribution at ice interface with liquid phase in frozen electrolyte as evaluated by
860 fluorometric measurements of pH. J. Phys. Chem. C. **118**, 15723-15731.
861 Yada T., Floss C., Stadermann F. J., Zinner E., Nakamura T., Noguchi T. and Lea S. (2008)
862 Stardust in Antarctic micrometeorites. *Meteorit. Planet. Sci.* **43**, 1287-1298.
863 Yurimoto H., Nagashima K. and Kunihiro T. (2003) High precision isotope micro-imaging of
864 materials. *Appl. Surf. Sci.* **203-204**, 793-797.
865 Zolensky M. E., Barrett B. and Browning L. (1993) Mineralogy and composition of matrix
866 and chondrule rims in carbonaceous chondrites. *Geochim. Cosmochim. Acta* **57**, 3123–
867 3148.
868 Zolensky M. E. and Barrett R. A. (1994) Composition variations of olivines and pyroxenes in
869 chondritic interplanetary dust particles. *Meteoritics* **29**, 616–620.
870 Zolensky M. et al. (2006) Mineralogy and petrology of comet Wild 2 nucleus samples.
871 *Science* **314**, 1735–1739.
872

873 **Figure captions:**

874

875 Figure 1. (a) Secondary electron image of an ultracarbonaceous micrometeorite (UCAMM)
876 D05IB80 placed on a platinum plate. The upper half of the UCAMM is porous and covered
877 by fine-grained (typically sub μm) particles, whereas the lower half is smooth. (b) Bright-field
878 (BF) TEM images of ultramicrotomed sections of the UCAMM D05IB80. Each section was
879 selected out of every three to five serial sections. Abbreviations: LPx , low-Ca pyroxene; PO,
880 pyrrhotite; Ol, Olivine.

881

882 Figure 2. (a, b) BF-TEM images of GEMS grains in the UCAMM D05IB80. (c)
883 HAADF-STEM image and elemental distribution maps of the same GEMS grains in (b). (d-i)
884 BF TEM images of minerals in a FIB section and ultrathin sections of D05IB80. (d) olivine
885 crystal in the FIB sections, (e-i) olivine, low-Ca pyroxene, high-Ca pyroxene, amorphous
886 silica, and pyrrhotite in ultrathin sections. An inset in each TEM image is a selected area
887 electron diffraction (SAED) pattern of each phase.

888

889 Figure 3. Chemical compositions of phases in the UCAMM D05IB80. (a) [Si + Al]-Mg-Fe

890 ternary diagram and (b) Si-S-Fe ternary diagram of GEMS grains. (c) Pyroxene quadrilateral
891 showing chemical compositions of low- and high-Ca pyroxenes and Forsterite (Fo) mol.%
892 histogram of olivine. (d) S-Fe-Ni ternary diagram of pyrrhotite. (e) FeO vs MnO and (f) FeO
893 vs Cr_2O_3 diagrams of olivine and low-Ca pyroxene.
894
895 Figure 4. BSE image after SIMS analysis and $^{12}C^{14}N^-$, $^{16}O^-$ and $^{32}S^-$ isotopographs of UCAMM
896 D05IB80.
897
898 Figure 5. (a) Back-scattered electron image, (b) optical image by a transmitted light, and (c)
899 that by a reflected light of the surface of the polished cross-section of the UCAMM D05IB80.
900 Tungsten deposition shown in (a) is the position where the focused ion beam (FIB) section
901 was lifted out. (c) Transmitted optical image of the FIB section of the UCAMM D05IB80.
902 The dark brown and the light brown area are contacted with a sinuous boundary. (d)
903 High-angle annular dark-field scanning transmission electron microscopy (HAADF-STEM)
904 image of the FIB section of D05IB80, where parallel grooves running from upper right to
905 lower left are tracks formed by Cs^+ ion implantation during the SIMS mapping analysis. The
906 two morphologies (smooth and globular) are indicated by arrows. Two box areas indicate

where elemental maps and high-resolution observation were performed (Fig. 9). Two GEMS grains and a polycrystalline olivine are also indicated.

Figure 6. Raman spectrum of the organic material in the UCAMM D05IB80. Background was subtracted. Peak position and full width at the half maximum (FWHM) of D_1 and G bands are shown as ω_{D1}, Γ_{D1}, ω_G, and Γ_G, respectively. In this spectrum, D_1 (red line), D_2 (green line), and G (blue line) bands were used to fit the spectrum. The residual graph is a difference between the raw spectrum and fitted spectrum.

Figure 7. (a) Carbon- and (b) nitrogen- distribution maps of the UCAMM D05IB80 obtained by STXM, and (c) carbon- and (d) nitrogen-XANES spectra of the regions 1, 2, and epoxy indicated in (b). Peak assignments are based on Leinweber et al. (2007) and Cody et al. (2008); peak A: 1s-π* transition for aromatic carbon (C=C*) at 285.1 eV, peak B: 1s-π* transition for N-heterocycles (C-N*=C), nitrile (C≡N*) or vinyl-keto carbon (C=C-C*=O) at ~286.6 eV, peak C: 1s-3p/s* transition for aliphatic carbon at CHx-C at ~287.5 eV, peak D: 1s-π* transition for carbonyl carbon in amide (NHx(C*=O)C) at ~288.0-288.2 eV and/or 1s-π* transition for carbonyl carbon in carboxyl or ester (OR(C*=O)C) at ~288.4-288.7 eV,

924 peak E: 1s-π* transition for imine (C=N*) at 398.8 eV, peak F: 1s-π* transition for
925 N-heterocycles (C-N*=C) and/or nitrile (C≡N*) and/or at ~399.7 eV, and peak G: 1s-π*
926 transition for amide (N*Hx(C=O)C) or 1s-3p/s* transition for amino (C-N*Hx) at 401.5 eV.
927
928 Figure 8. (a) BF TEM images obtained by in-situ observation of organic nanoglobules in the
929 UCAMM D05IB80. (b) Moderate- and (c) high-resolution BF TEM images of the globular
930 boundaries. (d) Moderate- and (e) high-resolution BF TEM images of the smooth boundary.
931 Thin (< 2 nm) less-electron transparent layers indicated by arrows exist on the both kinds of
932 boundaries shown in (c) and (e). (f) High-resolution TEM image of the thin layer in the
933 globular boundary shows nanocrystals indicating 0.24- and 0.28- nm lattice fringes. (g)
934 High-resolution TEM image of the thin layer in the smooth region shows there are no
935 nanocrystals in the boundary.
936
937 Figure 9. (a) Elemental distribution maps of the smooth boundary shown as “Map 1” in Fig.
938 5e. The area near the boundary is enriched in C, O, Na, Si, S, K, and Fe. (b) Elemental
939 distribution maps of the globular boundary shown as “Map 2” in Fig. 5e. The area near the
940 boundary is enriched in C, O, Si, S, and Fe. The less electron transparent material is enriched

941 in O, Si, S, and Fe. A GEMS grain appears as an O, Mg, and Si enriched area in the lower
942 right corner. (c) High resolution TEM image of a polycrystalline aggregate of tiny crystals
943 included in a globule. The tiny crystals show 0.46- and 0.24- nm lattice fringes.
944
945 Figure 10. (a) The $^{12}C^{14}N^-$ and δD isotopographs before preparing a FIB thin section. Scale
946 bars are 10 μm. Color bars are secondary ion counts for $^{12}C^{14}N^-$ isotopograph and isotope ratio
947 with delta-value for δD isotopograph. (b) BSE image, $^{12}C^{14}N^-$, $\delta^{13}C$ and $\delta^{15}N$ isotopographs
948 after making FIB thin section. Scale bars are 10 μm. Color bars are secondary ion counts for
949 $^{12}C^{14}N^-$ isotopograph and isotope ratio with delta-value for $\delta^{13}C$ and $\delta^{15}N$ isotopograph.
950
951 Figure. 11. N/C versus O/C ratios of organics in the UCAMM D05IB80 (●, this study), the
952 comet Wild 2 dust particles (□, Cody et al. 2008), the anhydrous IDP L20211R11 (■, Cody
953 et al. 2008), types 1 and 2 chondritic insoluble organic solids (■, Alexander et al. 2007), and
954 the UV irradiation products from interstellar analogues (O, Nuevo et al. 2011) (UV1
955 H_2O:CH_3OH:CO:NH_3 = 100:50:1:1, UV2 H_2O:CH_3OH:CO:NH_3:C_3H_8 = 100:50:1:1:10). The
956 ratios were estimated from fitting of C-, N-, and O-XANES spectra.
957

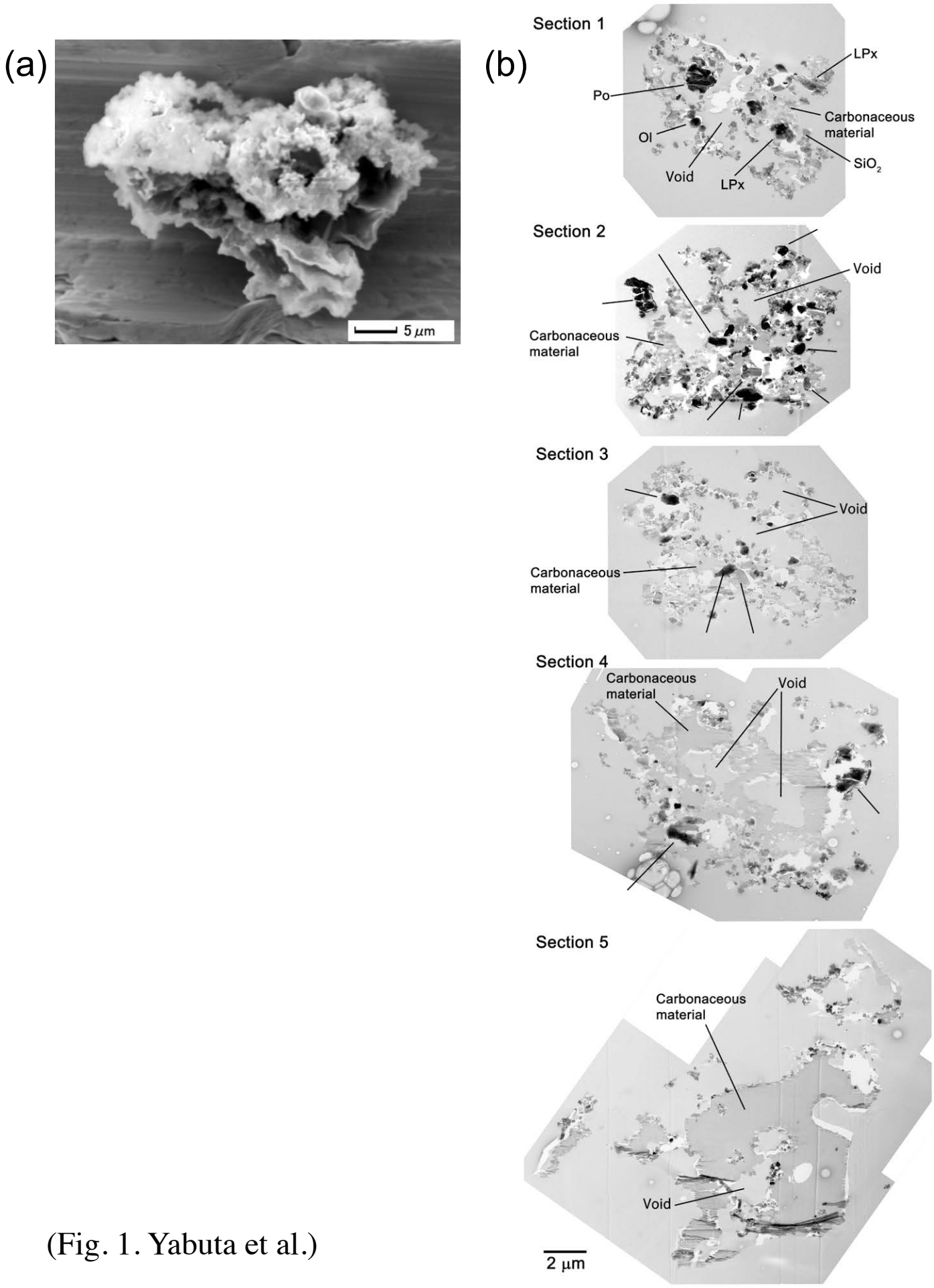

(Fig. 1. Yabuta et al.)

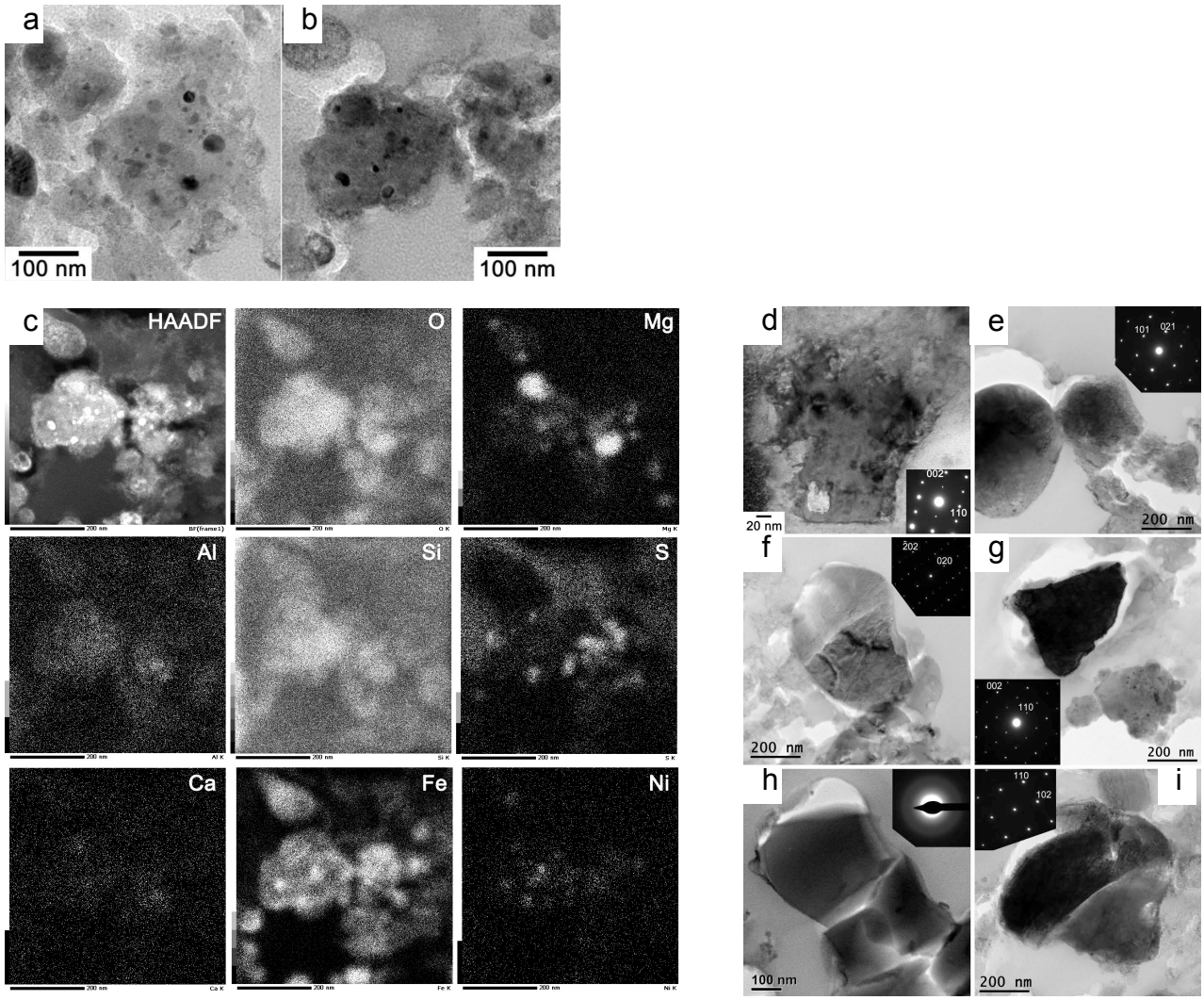

(Fig. 2. Yabuta et al.)

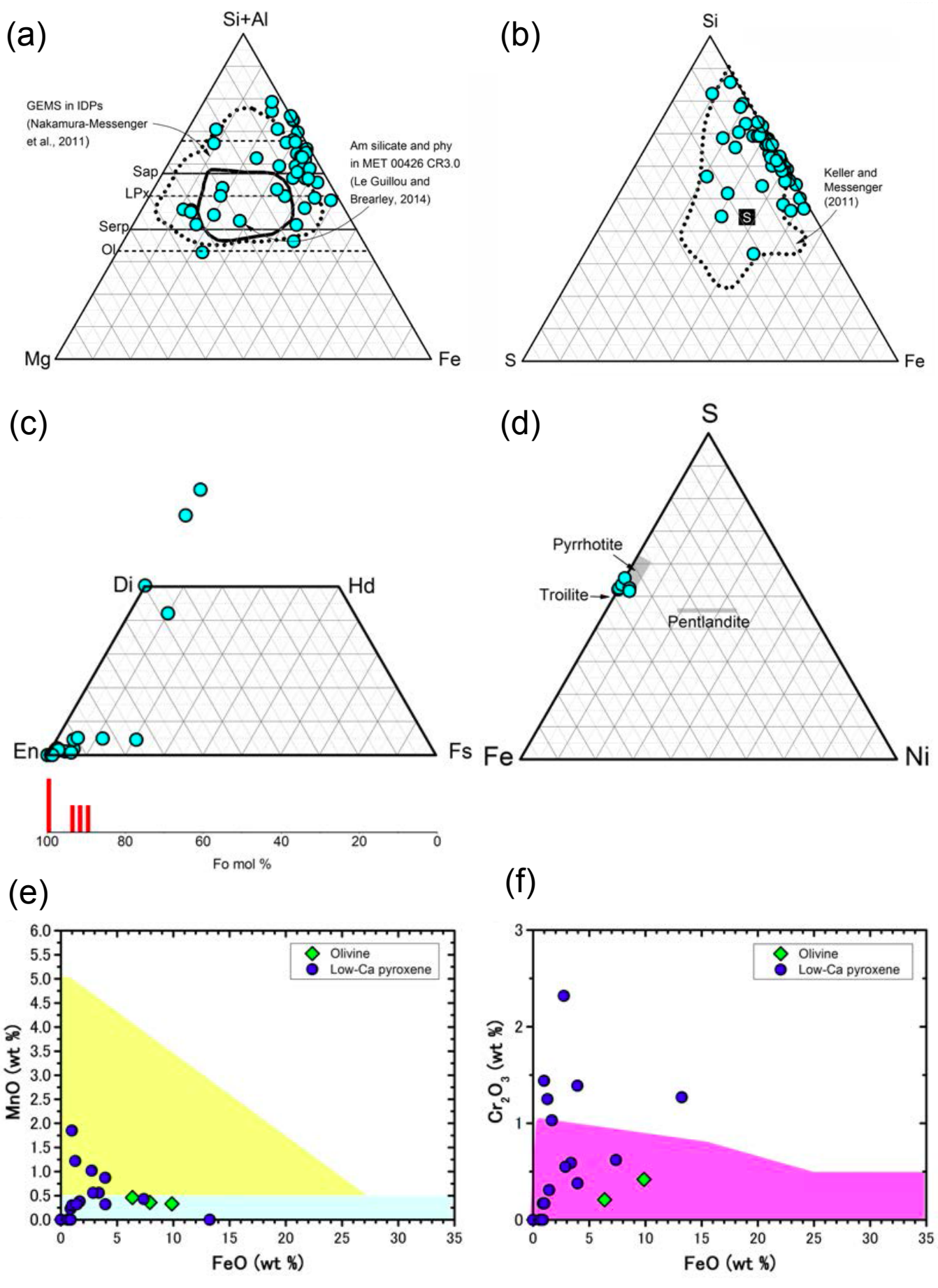

(Fig. 3. Yabuta et al.)

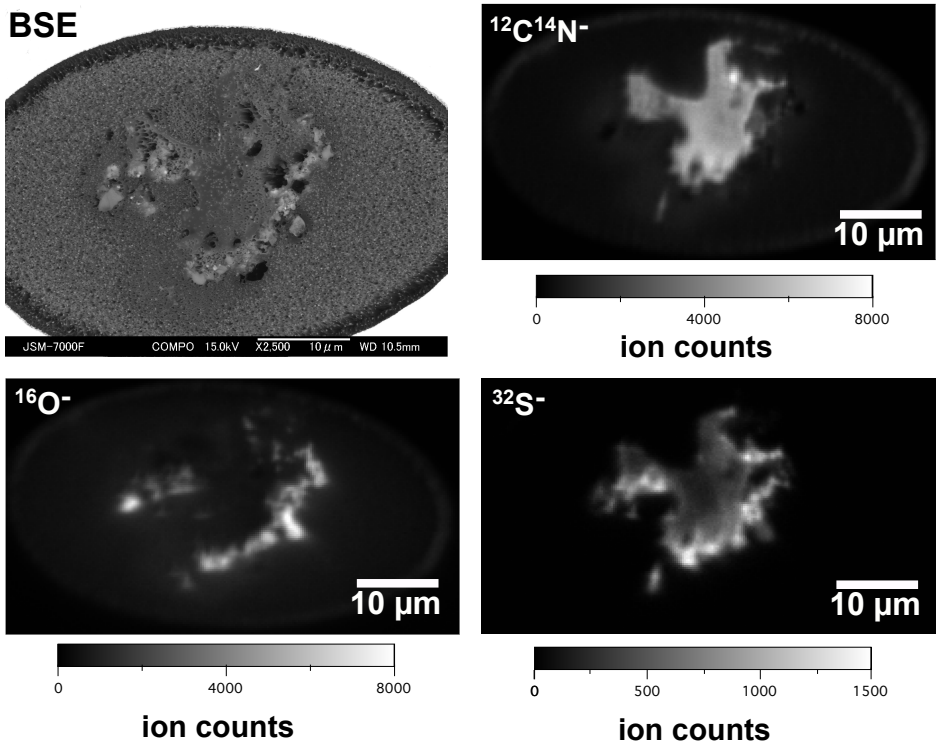

(Fig. 4. Yabuta et al.)

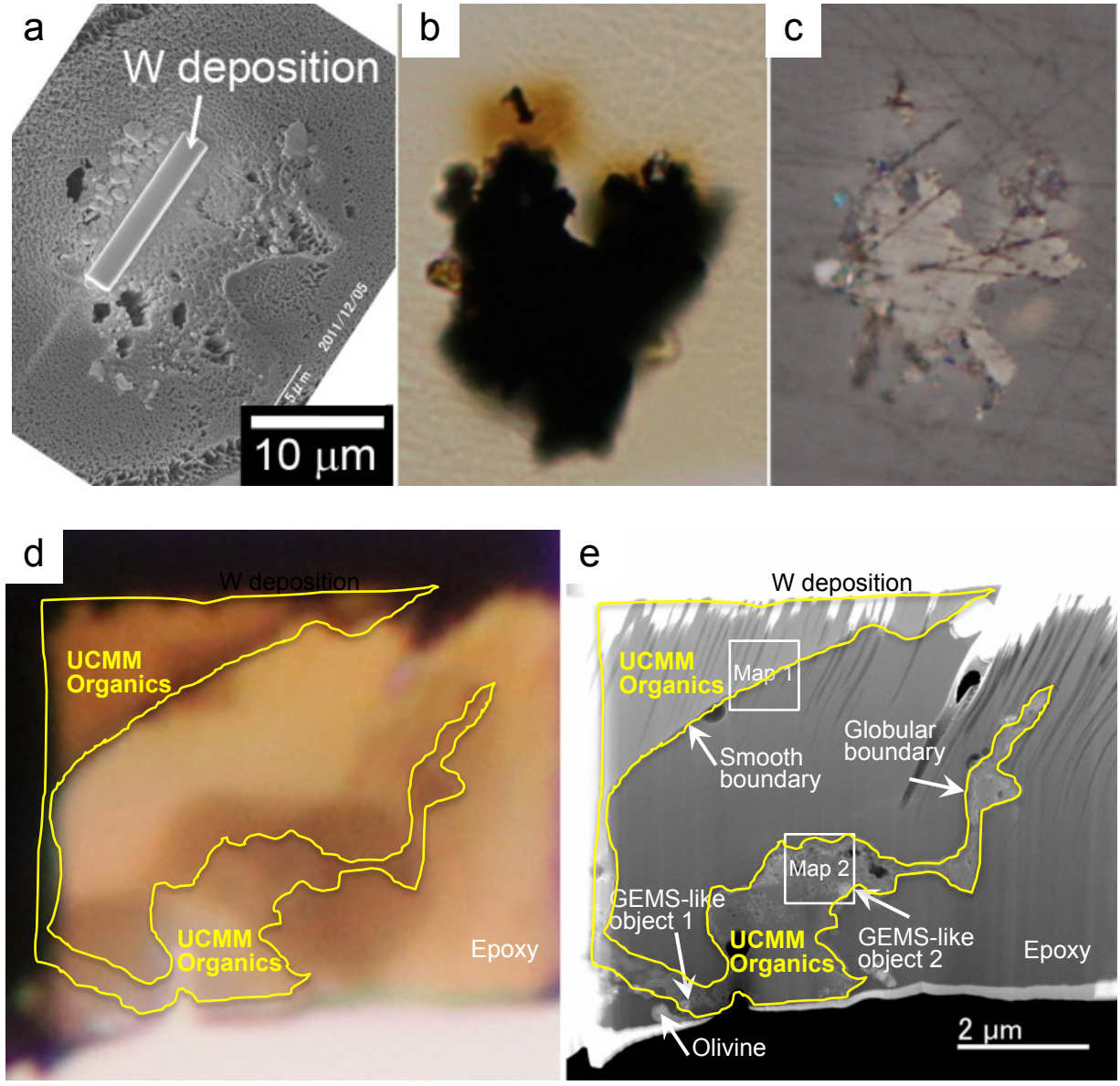

(Fig. 5. Yabuta et al.)

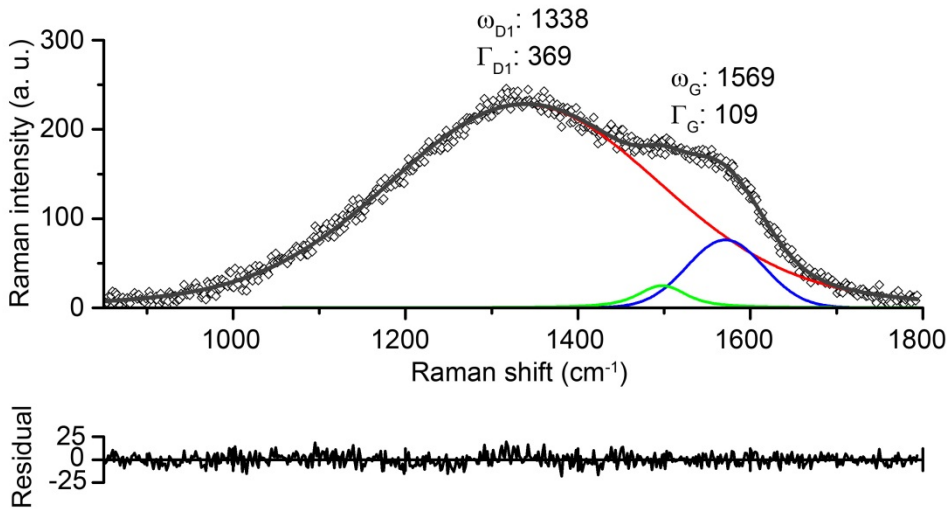

(Fig. 6. Yabuta et al.)

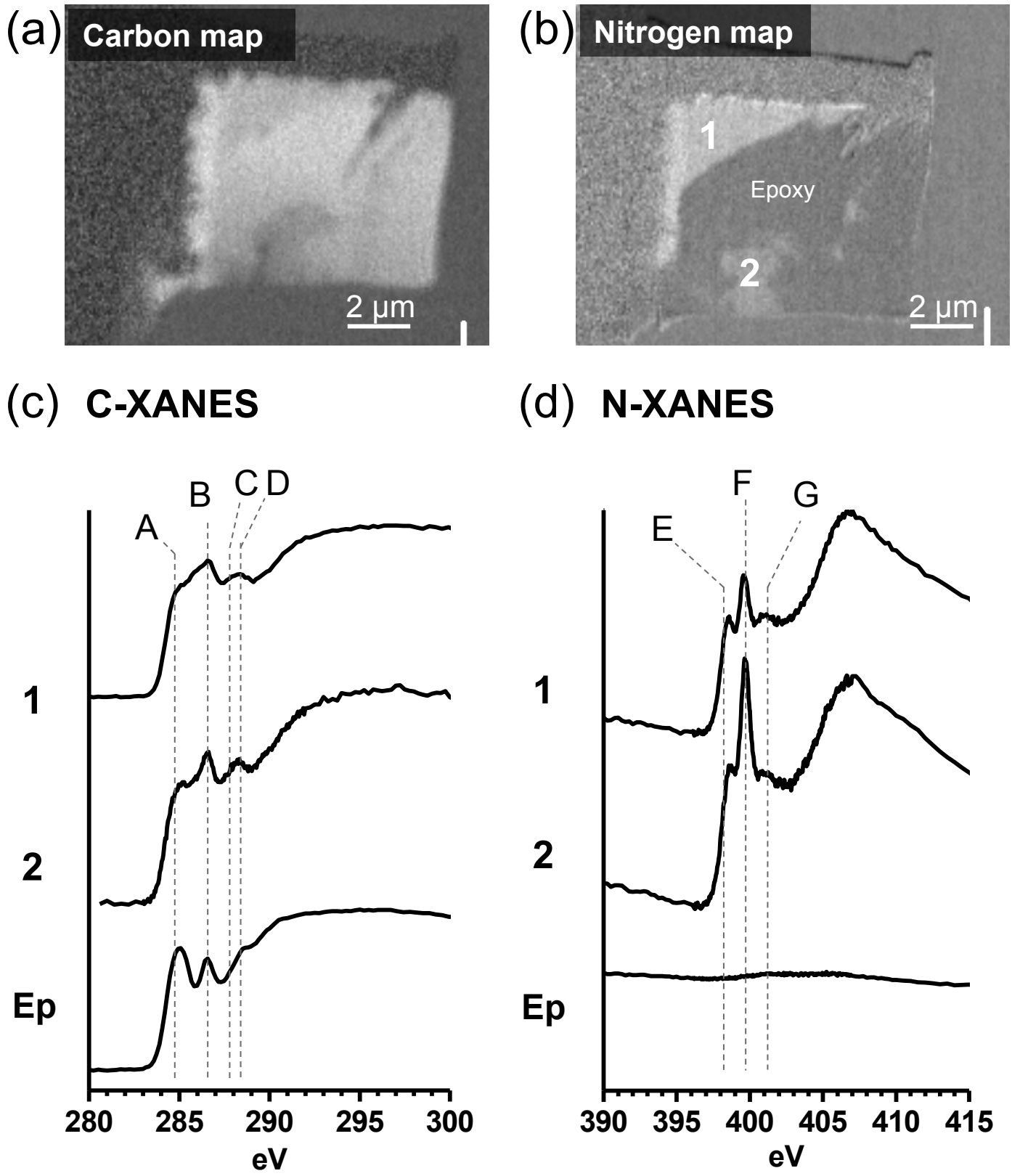

(Fig. 7. Yabuta et al.)

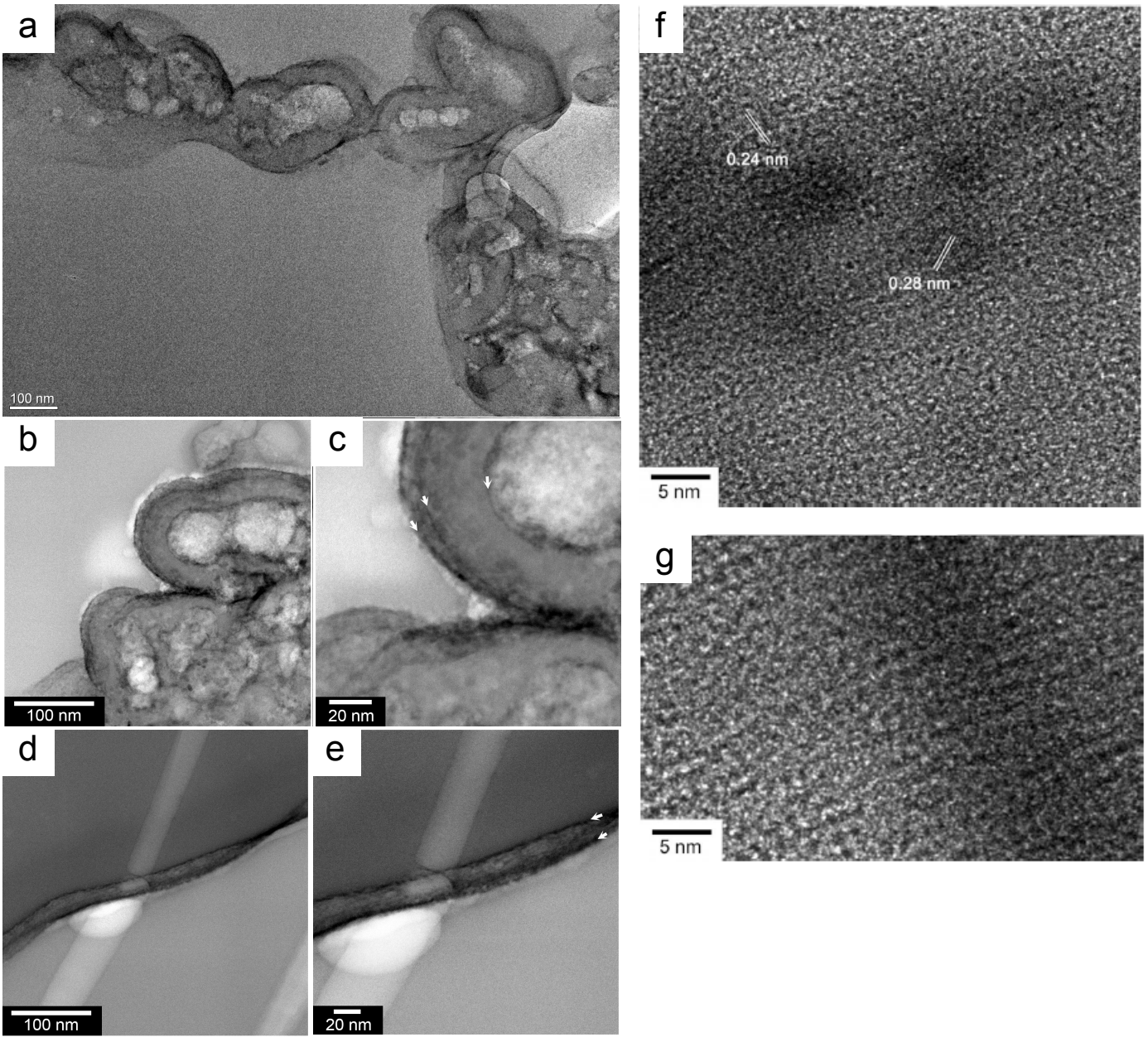

(Fig. 8. Yabuta et al.)

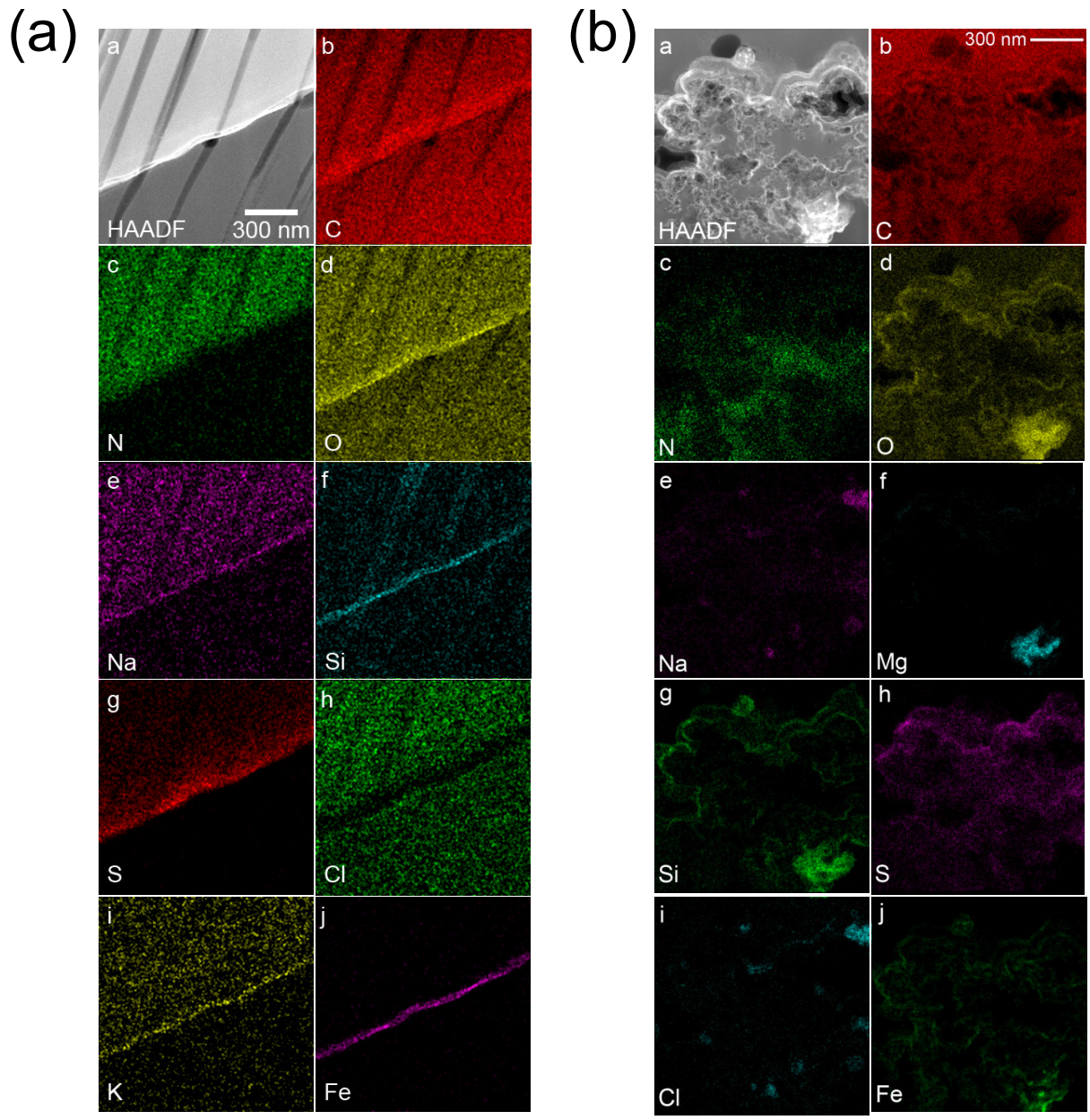

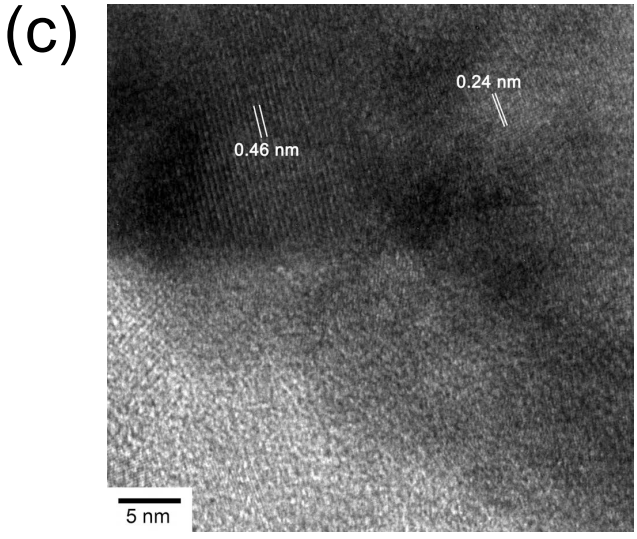

(Fig. 9. Yabuta et al.)

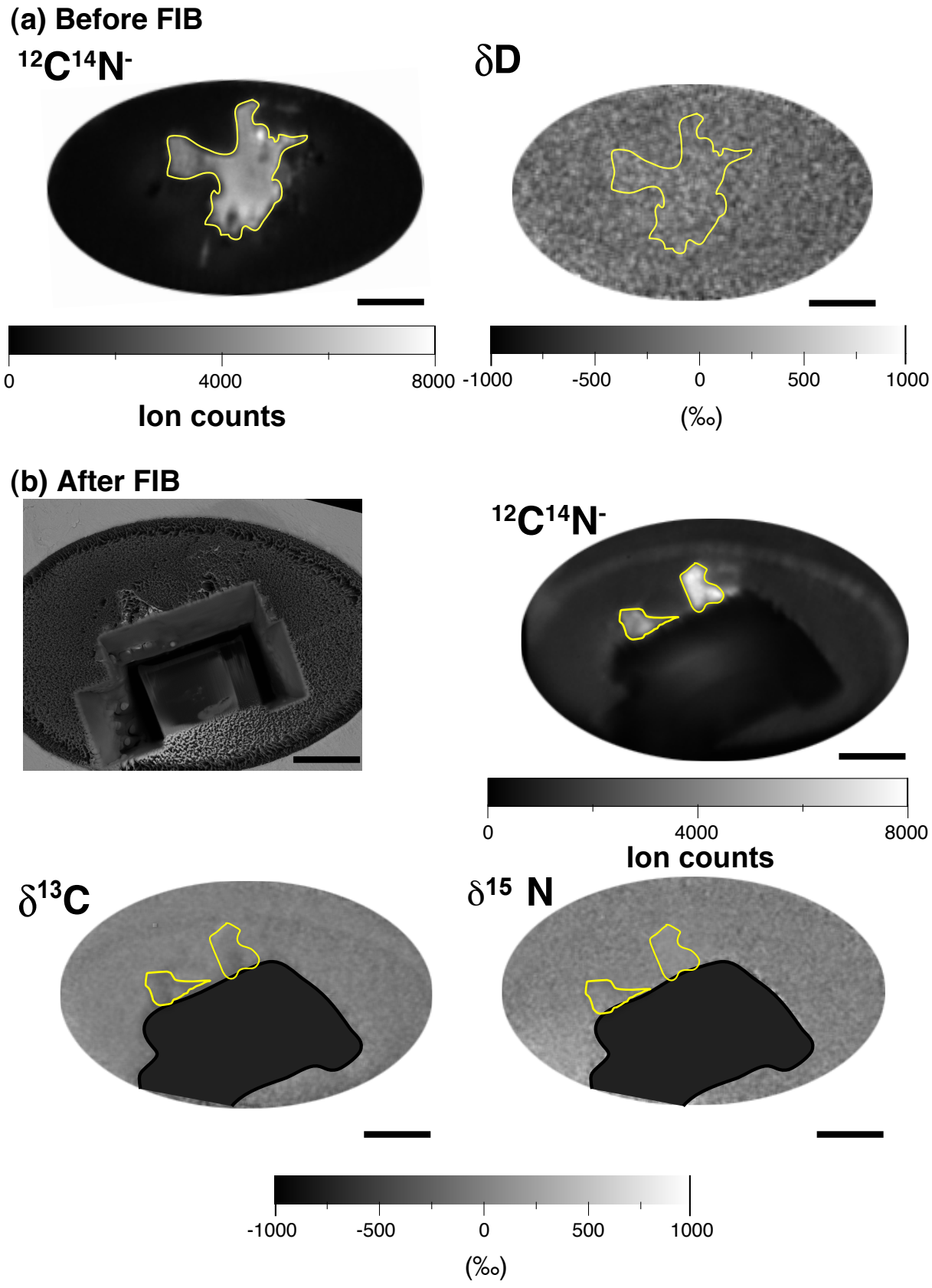

(Fig. 10. Yabuta et al.)

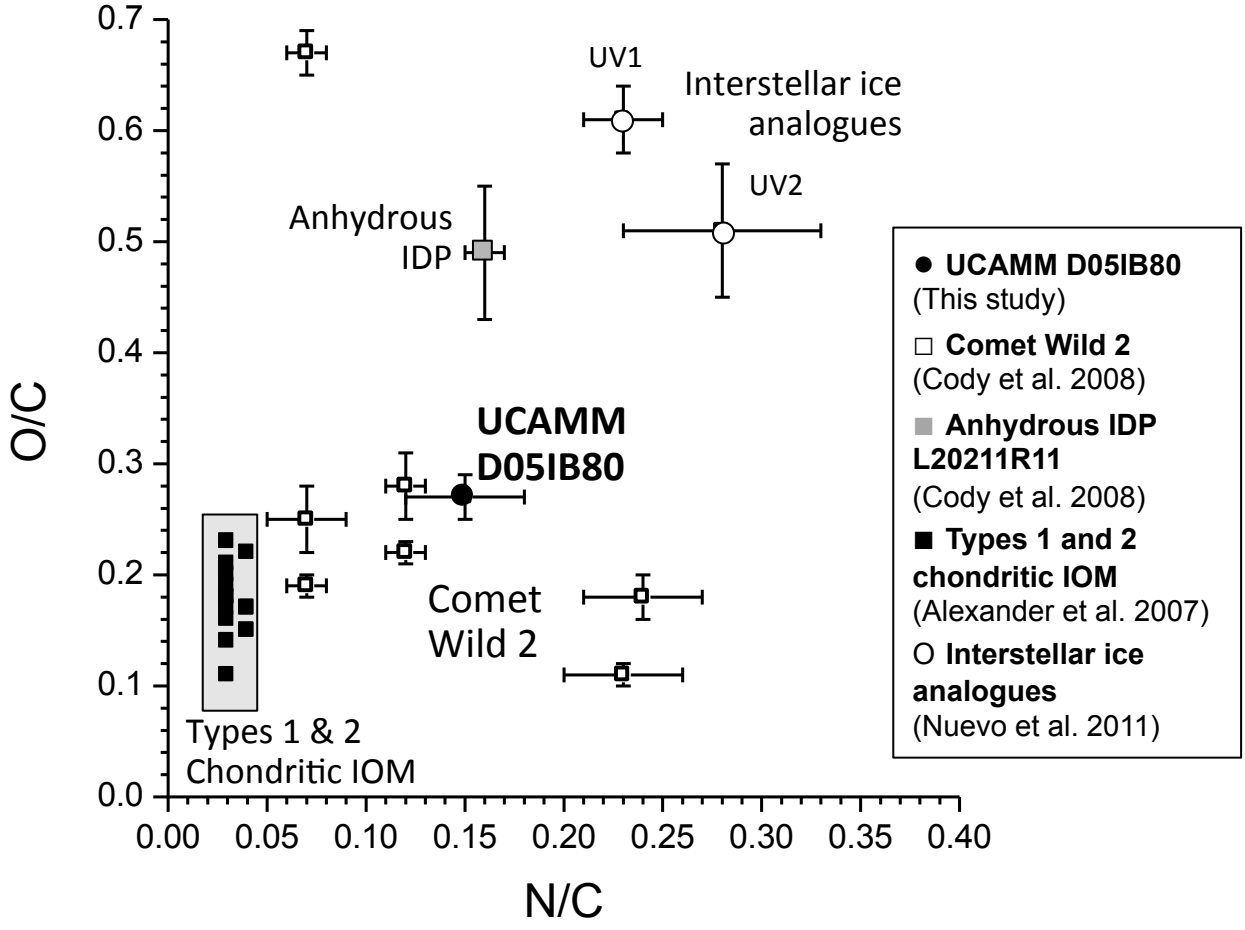

(Fig. 11. Yabuta et al.)